

JWST View of the Supernebula in NGC 5253. II. Nebular Lines

Downloaded from: https://research.chalmers.se, 2026-11-23 12:15 UTC

Citation for the original published paper (version of record):
Beck, S., Turner, J., Zweig, E. et al (2026). JWST View of the Supernebula in NGC 5253. II. Nebular Lines. Astrophysical Journal, 1011(2). http://dx.doi.org/10.3847/1538-4357/ae8519

N.B. When citing this work, cite the original published paper.

research.chalmers.se offers the possibility of retrieving research publications produced at Chalmers University of Technology. It covers all kind of research output: articles, dissertations, conference papers, reports etc. since 2004. research.chalmers.se is administrated and maintained by Chalmers Library

(article starts on next page)

The Astrophysical Journal, 1011:204 (23pp), 2026 November 10 https://doi.org/10.3847/1538-4357/ae8519
© 2026. The Author(s). Published by the American Astronomical Society.
OPEN ACCESS

JWST View of the Supernebula in NGC 5253. II. Nebular Lines

Sara C. Beck[1], Jean L. Turner[2], Elm Zweig[2], John H. Black[3], Paul T. P. Ho[4], David S. Meier[5], Sergiy Silich[6,7], Daniel P. Cohen[2], S. Michelle Consiglio[2], and Nicholas G. Ferraro[2]
[1] School of Physics and Astronomy, Tel Aviv University, Israel
[2] Department of Physics and Astronomy, UCLA, Los Angeles, CA 90095, USA
[3] Department of Physics and Astronomy, Chalmers Institute of Technology, Gothenberg, Sweden
[4] Academia Sinica Astronomy and Astrophysics, Taiwan
[5] New Mexico Institute of Mining and Technology, Socorro, NM 87801, USA
[6] Instituto Nacional de Astrofísica Óptica y Electrónica, Mexico
Received 2025 November 12; revised 2026 June 22; accepted 2026 June 30; published 2026 November 4

Abstract

The nearby dwarf starburst NGC 5253 is dominated by a compact radio-infrared supernebula powered by a very young and bright embedded super star cluster of $\sim 10^9\ L_\odot$. We observed this source and its surroundings over the 5–25 μm range with the Mid-Infrared Instrument (MIRI) Medium Resolution Spectrometer (MRS) on JWST, and in Paper I presented the JWST view of the region and its continuum features. We now present the more than 70 emission lines of H I, H_2, and metal ions detected by MIRI/MRS. We derive the extinction by comparing H I recombination lines to the free–free radio continuum and find that it is very flat, i.e., almost independent of wavelength over this spectral range. Nebular conditions are consistent with young ($\lesssim 5 \times 10^6$ yr) and very massive stars. All regions show high excitation, but the spatial distribution of the high-excitation lines suggests that photons with energies close to 50 eV are escaping the supernebula core in spite of 35 mag of visual extinction.

Unified Astronomy Thesaurus concepts: Blue compact dwarf galaxies (165); Starburst galaxies (1570); Infrared spectroscopy (2285); James Webb Space Telescope (2291); Young massive clusters (2049)

1. Introduction

This is the second in a series of papers reporting on a project of 5–28 μm spectroscopy of the starburst in the nearby ($D = 3.7$ Mpc) dwarf galaxy NGC 5253, carried out with the Mid-Infrared Instrument (MIRI) Medium Resolution Spectrometer (MRS) spectrometer on JWST. In J. L. Turner et al. (2026, hereafter Paper I), the data reduction and analysis are described in detail and the main features of the infrared continuum are discussed. In this paper, we present the rich variety of emission lines that dominate the mid-infrared (MIR) spectra and analyze the overall picture of extinction, temperature, and ionization in the starburst.

NGC 5253 is a much studied and remarkable source. The NGC 5253 starburst is noteworthy because of its location in a low-metallicity ($\sim$0.2–0.3 $Z_\odot$) galaxy (J. R. Walsh & J.-R. Roy 1989; H. A. Kobulnicky et al. 1997; A. Monreal-Ibero et al. 2010), its youth (the brightest star cluster is estimated to be less than 1.5–3.5 Myr years old; A. Alonso-Herrero et al. 2004; J. Harris et al. 2004; D. Calzetti et al. 2015), and its intensity (A. Alonso-Herrero et al. 2004; J. L. Turner & S. C. Beck 2004; C. A. Rodríguez-Rico et al. 2007; G. J. Bendo et al. 2017; S. M. Consiglio et al. 2017). The radiation fields and temperatures in this region must be extreme, approaching conditions of the first starbursts in the early Universe. The embedded cluster that dominates the radio-infrared luminosity is a good candidate for a protoglobular cluster, and the galaxy as a whole is a possible Local Universe analog to starbursts at Cosmic Noon.

The starburst in NGC 5253 is a complex region holding many star clusters, gas, and dust features; it has significant obscuration and the optical appearance is strongly affected by extinction. This paper will concentrate on four sources of particular interest, which we believe, from the infrared continuum results of Paper I and other observations, to be embedded star clusters. These sources are introduced and briefly discussed in Section 3.

In the next section we review and summarize the new JWST observations of NGC 5253, the data reduction process, and the data quality. Section 3 describes the regions of special interest and introduces the rich emission-line spectrum detected by JWST. In Section 4 we use the H I recombination lines to derive and discuss the extinction to the NGC 5253 starburst. Section 5 introduces the fine-structure emission lines of metal ions that dominate the MIR spectrum and discusses the radiation field that creates them, their role in cooling, and what they suggest about the stellar populations of the embedded star clusters and the escape of photons therefrom.

2. Data Analysis and Reduction

Reduction and analysis of the JWST data presented many challenges, which are discussed in detail in Paper I. We review the process here briefly and refer the reader to Paper I for details.

A single science pointing of the MIRI/MRS spectrometer and a dedicated background were observed in 2022 March for Program JWST-GO-4302 (PI: J. Turner). Data were obtained for each of the short, medium, and long grating settings in all four channels of the spectrometer, for a total of 12 bands covering wavelengths 4.98–28 μm. The spatial resolution ranges from FWHM = 0.″3 at the shortest wavelength to 0.″9

[7] Deceased.

Original content from this work may be used under the terms of the Creative Commons Attribution 4.0 licence. Any further distribution of this work must maintain attribution to the author(s) and the title of the work, journal citation and DOI.

at the longest, and the spectral resolution from $R = 1300$ to 3700 (I. Argyriou et al. 2023a).

NGC 5253 required special approaches to data reduction because of the extreme infrared brightness of the central source, which caused spectral "fringing" so strong that the STScI defringing routine cannot completely remove it. There are also spatial artifacts such as the "petals" of the point-spread function (PSF) and the "cruciform" (A. Gáspár et al. 2021) that affect nearly the entire field of view. In addition, the background pointing was found to have significant continuum and line emission, so we created a custom background for subtraction, which is described in Paper I.

Since defringing is more effective on 1D spectra than 3D cubes, we defined regions to serve as effective apertures for extraction of spectra. The starburst is a combination of compact sources and extended emission, so we use fixed apertures rather than "cones" to analyze fluxes. Following the recommendation that apertures larger than the PSF be used to compensate for known artifacts in MRS cubes (I. Argyriou et al. 2023b; D. R. Law et al. 2023; D. Dicken et al. 2024), our apertures have typically $r \gtrsim 0\farcs8$, giving a diameter approximately twice the FWHM at $\lambda \sim 20\ \mu$m, which should render resampling noise negligible (D. R. Law et al. 2023). We used these apertures for the regions to extract spectra in CARTA by summing intensities using the "SUM" statistic. These intensity sums were converted to Jy using the header parameter, PIXAR, which describes the solid angles of pixels for the individual bands. These converted 1D region spectra were then defringed using the algorithm from `jwst.residual_fringe.utils`.

Lines were identified by eye in the defringed 1D spectra and fit with the `Specviz` Gaussian procedure to give fluxes, centroids, and errors. Velocity centroids were checked to assure correct line identification. Lines of lower signal-to-noise ratio (S/N) showed more velocity shifts, as expected from the $\sim$100 km s^{-1} resolution of the spectrometer, but even these were typically within 10–15 km s^{-1} of the expected velocity of NGC 5253.

The greatest source of uncertainty in the line fluxes is the definition of the underlying continuum baseline, which is often affected by residual fringing. For nearly all lines the default Specviz "surroundings" baseline was used. For a limited number of closely spaced lines, we defined a custom baseline. The uncertainties shown in Table 1 were estimated by duplicating the Gaussian fit with the same bandwidth and baseline-subtraction parameters on a nearby line-free section of continuum. They do not include aperture correction or the estimated 4%–5% uncertainty in the absolute flux calibration of MIRI/MRS. While we did not use the cubes for fitting spectra due to the fringing, we note that the uncertainties given by `Cubeviz` and by Gaussian fit routines in CARTA for the line fits are typically smaller than what we have adopted here. The uncertainties we list for the line fluxes are from the fits and do not include systematics such as baseline, photometric, or aperture uncertainties.

We established International Celestial Reference System (ICRS) coordinates for the cubes by comparing to a high-resolution map from the Atacama Large Millimeter/submillimeter Array (ALMA) archive (Project 2017.1.00964.S, PI: D. Nguyen) of the 1.3 mm continuum. The 1.3 mm continuum in NGC 5253 is consistent with free–free emission (D. S. Meier et al. 2002; C. A. Rodríguez-Rico et al. 2007); although G. J. Bendo et al. (2017) suggest that the 1.3 mm may include some dust emission, that will not affect the overall registration of the maps. The astrometry is estimated to be good to $\lesssim$50 mas. Comparisons with radio continuum are estimated to be good to $\sim$50 mas.

For a few lines, continuum-free line images were constructed. For each line, a range of pixels slightly larger than the line width was computed on either side of the line using the MOM3 function of CARTA (median) to obtain a continuum intensity image. Line-plus-continuum images were done with the MOM8 function (peak intensity), with the spectral range specified to isolate the line, 3–6 pixels in extent. For high-S/N unresolved lines, the MOM8 images, in units of MJy sr^{-1}, will be proportional to the line flux. Continuum images were subtracted from the MOM8 maps to give continuum-free line images.

3. The H II Regions of the NGC 5253 Starburst Region

In Paper I, we established the presence of four continuum features within the $\sim$120 pc MIRI/MRS footprint. We defined regions NGC 5253-D1, NGC 5253-D2, NGC 5253-D4, and NGC 5253-D6 as effective apertures centered on these MIR continuum features from which spectra were extracted. These regions were defined to be large enough to minimize artifacts and allow defringing. The continuum features and region definitions were discussed in Paper I.

These four continuum regions are displayed in Figure 1, along with maps of the Hα emission from the 656N HST image (D. Calzetti et al. 1997), the ALMA CO(3–2) image, which measures warm dense molecular gas (S. M. Consiglio et al. 2017; J. L. Turner et al. 2017), and an ALMA 107 GHz continuum image, which is largely free–free emission (D. S. Meier et al. 2002; C. A. Rodríguez-Rico et al. 2007). The region names refer to CO clouds identified in S. M. Consiglio et al. (2017), although the JWST apertures are larger than the clouds, $\sim1\farcs2$–$1\farcs6$ in size, and not centered on them. Two other regions are defined: "Ellipse," which encompasses the plumes seen in Hα to the northwest and southeast and omits D2 and D6, and "Chip," which covers the minimum MIRI/MRS footprint at 5 μm.

Figure 1 shows that the Hα does not agree well with the strongest radio free–free continuum emission. This and other evidence argues that the optical appearance is strongly affected by extinction and that the radio continuum is the more reliable probe of the ionized gas.

The D1, D2, D4, and D6 sources are all associated with molecular gas, ionized gas, and dust continuum emission and presumably hold embedded H II regions. Region D1 contains the powerful core of the supernebula, a very strong radio source that dominates the centimeter-wave emission of the starburst. The 7 mm radio flux (C. A. Rodríguez-Rico et al. 2007) indicates that the region requires an ionization rate of $Q_o \sim 7.7 \times 10^{52}$ s^{-1}; 40% of the radio flux emerges from a $\sim$5 pc region, which presumably contains the cluster powering the radio core and larger nebula.

This ionization requires $\gtrsim$1000 O stars within a subarcsecond, parsec-scale core (J. L. Turner & S. C. Beck 2004). The star cluster is mixed with hot CO gas (S. M. Consiglio et al. 2017; J. L. Turner et al. 2017). It is not visible at optical wavelengths (L. J. Smith et al. 2020), but the continuum source coincident with the H II region becomes apparent in the near-infrared (NIR; A. Alonso-Herrero et al. 2004;

Table 1
Line Fluxes in NGC 5253

		D1		D2		D4		D6		Ellipse		Chip	
λ_{rest}	Line	v [a]	Flux[b]	v	Flux	v	Flux	v	Flux	v	Flux	v	Flux
4.9237	H I 23–7	399	1.4 (0.2)	…	…	…	…	…	…	…	…	…	…
4.9709	H I 22–7	362	1.1 (0.2)	…	…	…	…	…	…	386	1.0 (1.0)	374	1.4 (1.0)
4.9938	UIA	433	-1.5 (0.3)	…	…	…	…	…	…	390	−1.5 (1.0)	…	…
5.0261	H I 21–7	372	1.2 (0.3)	…	…	387	0.28 (0.3)	…	…	387	2.1 (1.0)	379	1.6 (1.0)
5.1287	H I 10–6	379	14 (0.1)	361	0.96 (0.1)	370	1.7 (0.2)	361	1.8 (0.1)	382	19 (0.7)	375	22 (1.0)
5.1693	H I 19–7	343	1.2(0.1)	…	…	…	…	…	…	402	1.4 (0.7)	407	2.2 (1.0)
5.2637	H I 18–7	398	1.1 (0.2)	…	…	…	…	…	…	401	2.4 (0.7)	401	2.9 (1.0)
5.3402	[Fe II]	409	12 (0.3)	379	2.6 (0.2)	388	3.6 (0.1)	385	4.4 (0.2)	392	27 (0.7)	388	45 (1.0)
5.3798	H I 17–7	366	1.7 (0.3)	…	…	…	…	…	…	366	4.2 (0.7)	380	4.3 (1.0)
5.4650	UIL	371	0.72 (0.3)	…	…	…	…	284	0.7 (0.2)	…	…	…	…
5.5112	H_2 S(7)	381	0.95 (0.3)	…	…	375	0.67 (0.2)	425	0.3 (0.1)	385	1.5 (0.7)	434	1.6 (0.7)
5.5252	H I 16–7	364	2.4 (0.3)	…	…	…	…	…	…	386	4.2 (0.7)	391	4.7 (0.7)
5.6925	H_2CO	433	−1.4 (0.5)	…	…	…	…	…	…	390	−2.1 (0.7)	372	−4.2 (0.7)
5.7115	H I 15–7	366	2.6 (0.2)	…	…	…	…	…	…	358	4.5 (0.5)	344	6.3 (1.0)
5.7514	H_2CO	359	−1.8 (0.2)	…	…	380	-0.7 (0.2)	…	…	380	−2.2 (0.5)	413	−2.4 (1.0)
5.9082	H I 9–6	380	21 (0.2)	382	1.0 (0.1)	399	2.2 (0.2)	403	1.5 (0.1)	373	30 (0.5)	368	34 (0.5)
5.9398	UIA	…	…	…	…	…	…	…	…	…	…	380	−3.0 (0.5)
5.9568	H I 14–7	385	3.5 (0.2)	…	…	387	0.22 (0.3)	…	…	377	5.2 (0.5)	384	6.3 (0.5)
5.9820	[K IV]	416	5.1 (0.2)	…	…	…	…	481	.74 (0.1)	429	6.8 (0.5)	425	6.4 (0.5)
6.2919	H I 13–7	352	5.1 (0.8)	…	…	375	0.67 (0.1)	361	0.7 (0.1)	365	7.7 (0.5)	363	8.1 (1.0)
6.4385	UIA	390	−0.8 (0.2)	…	…	…	…	…	…	…	…	…	…
6.6366	[Ni II]	323	2.8 (0.3)	340	0.43 (0.1)	…	…	…	…	385	4.7 (0.3)	505	5.3 (1.0)
6.7720	H I 12–7	358	5.6 (0.1)	388	0.35 (0.1)	369	0.60 (0.2)	416	0.6 (0.2)	358	7.9 (0.3)	391	10 (1.0)
6.9095	H_2 S(5)	399	2.3 (0.5)	393	0.36 (0.1)	391	0.80 (0.2)	398	0.6 (0.2)	396	4.4 (0.3)	396	7.6 (0.5)
6.9853	[Ar II]	381	30 (0.7)	391	3.4 (0.1)	395	6.0 (0.2)	404	6.4 (0.2)	387	57 (0.3)	389	78 (0.5)
7.3177	[Na III]	390	15 (0.5)	330	0.35 (0.1)	370	1.6 (0.5)	…	…	386	18 (1.0)	392	19 (0.5)
7.4599	H I 6–5	376	118 (0.5)	356	6.7 (0.1)	380	13 (0.4)	383	10.4 (0.1)	376	160 (1.0)	377	189 (0.6)
7.5025	H I 8–6	385	33(0.5)	393	1.7 (0.1)	399	3.5 (0.4)	403	3.1 (0.1)	387	42 (1.0)	389	51 (0.6)
7.5081	H I 11–7	394	8.8(0.5)	381	0.44 (0.1)	373	0.92 (0.4)	404	0.8 (0.1)	390	11 (1.0)	390	13 (0.6)
7.7804	H I 16–8	401	1.8 (0.2)	…	…	379	0.35 (0.4)	…	…	380	2.7 (0.2)	371	2.3 (1.0)
7.7840	UIL	…	…	…	…	414	0.38 (0.1)	…	…	…	…		
7.8790	UIL	…	…	309	0.35 (0.1)	398	0.33 (0.1)	400	0.5 (0.1)	387	3.4 (0.5)	452	8.6 (1.0)
8.0250	H_2 S(4)	382	0.8 (0.3)	492	0.44 (0.1)	413	0.47 (0.1)	400	0.3 (0.1)	391	1.5 (0.5)	405	3.2 (0.4)
8.1549	H I 15–8	402	1.1 (0.3)	…	…	…	…	375	0.4 (0.1)	378	1.9 (0.5)	364	2.9 (0.4)
8.3279	UIA	380	−0.7 (0.1)	…	…	…	…	…	…	398	−1.5 (1.0)	381	−1.7 (8.0)
8.4097	C I	385	3.1 (0.1)	…	…	389	0.38 (0.1)	…	…	382	4.5 (1.0)	385	6.0 (0.5)
8.6645	H I 14–8	402	1.2 (0.3)	…	…	380	0.36 (0.1)	452	0.4 (0.1)	378	2.6 (1.0)	380	3.3 (0.8)
8.7289	UIL	…	…	…	…	380	0.59 (0.0)	…	…	…	…	…	…
8.7601	H I 10–7	391	7.3 (0.3)	390	0.52 (0.1)	404	0.9 (0.1)	413	0.7 (0.1)	391	11 (0.7)	392	14 (0.7)
8.7882	UIA	326	−3.9 (0.3)	…	…	…	…	…	…	…	…	390	−4.3 (0.7)
8.9480	UIL	345	5.8 (0.3)	…	…	…	…	…	…	380	6.3 (0.7)	444	6.2 (0.7)
8.9914	[Ar III]	377	310 (0.9)	384	19 (0.1)	384	41 (0.0)	396	40 (0.1)	379	480 (0.4)	381	584 (0.6)
9.0998	UIL	…	…	356	1.2 (0.1)	388	0.86 (0.0)	391	1.2 (0.1)	380	8.3 (0.4)	386	15 (0.6)
9.3920	H I 13–8	373	1.2 (0.2)	…	…	362	0.16 (0.1)	…	…	375	1.9 (0.4)	381	2.0 (0.6)
9.6649	H_2 S(3)	388	2.0 (0.2)	383	0.58 (0.1)	395	1.4 (0.1)	399	1.3 (0.0)	390	5.8 (0.4)	389	8.9 (0.6)
10.5105	[S IV]	376	2301 (0.3)	362	76 (0.2)	380	275 (0.4)	394	134 (0.1)	375	3420 (0.5)	376	3860 (1.0)
10.8036	H I 16–9	…	…	…	…	…	…	…	…	…	…	388	0.5 (0.3)
11.3087	H I 9–7	379	11 (0.4)	371	0.75 (0.2)	384	1.2 (0.1)	394	0.9 (0.1)	383	16 (2.0)	385	20 (0.3)
11.5395	H I 15–9	382	1.7 (0.2)	…	…	…	…	…	…	385	1.5 (0.3)	389	2.0 (0.3)
11.6550	UIL	380	3.5 (0.5)	…	…	…	…	…	…	…	…	…	…
11.7619	[Cl IV]	392	3.8 (1.0)	…	…	402	0.87 (0.1)	409	0.4 (0.1)	386	6.7 (1.0)	396	6.6 (0.7)
12.2790	H_2 S(2)	376	2 (1.0)	364	0.44 (0.1)	405	1.9 (0.3)	390	0.8 (0.1)	365	5.1 (1.0)	377	5.3 (0.6)
12.3719	H I 7–6	387	39 (0.2)	385	2.2 (0.0)	381	6.7 (0.3)	398	4.0 (0.1)	382	61 (1.5)	380	76 (0.6)
12.3872	H I 11–8	413	5.1 (0.2)	418	0.27 (0.0)	430	0.91 (0.3)	405	0.4 (0.1)	394	4.9 (1.5)	423	11 (0.6)
12.5871	H I 14–9	392	1.7 (0.4)	…	…	…	…	399	0.12 (0.1)	380	2.0 (0.3)	395	2.8 (0.6)
12.6415	[Fe II]	365	1.4 (0.4)	…	…	366	0.33 (0.5)	…	…	364	1.4 (0.3)	361	1.4 (0.6)
12.8136	[Ne II]	380	167 (0.5)	396	20 (0.1)	398	40 (0.3)	405	46 (0.1)	394	305 (0.5)	396	434 (0.6)
13.4016	UIA	282	−0.7 (0.5)	…	…	…	…	…	…	…	…	390	-3.0 (0.5)
13.4037	UIA	390	−1.5 (0.5)	…	…	…	…	…	…	…	…	…	…
13.4490	UIA	…	…	…	…	…	…	…	…	…	…	390	−4.4 (0.5)
13.9619	UIA	…	…	378	−1.1 (0.1)	…	…	…	…	…	…	…	…
14.1830	H I 13–9	380	2.1 (0.2)	…	…	…	…	398	0.2 (0.1)	380	3.0 (0.3)	388	4.8 (0.3)
14.3217	[Ne V]	326	2.3 (0.2)	…	…	320	0.39 (0.1)	…	…	315	3.6 (0.3)	316	3.8 (0.3)

Table 1
(Continued)

		D1		D2		D4		D6		Ellipse		Chip	
λ_{rest}	Line	v [a]	Flux[b]	v	Flux	v	Flux	v	Flux	v	Flux	v	Flux
14.3678	[Cl II]	…	…	373	0.19 (0.0)	…	…	381	0.3 (0.01)	358	1.8 (0.4)	366	3.0 (0.3)
14.3795	UIA	394	−1.4 (0.3)	…	…	…	…	…	…	…	…	390	−2.7 (0.3)
14.6072	UIA	386	-4.7 (0.3)	…	…	…	…	…	…	390	−4.8 (0.4)	393	-5.2 (0.3)
15.5551	[Ne III]	404	1592 (0.7)	408	108 (0.0)	407	347 (0.1)	430	203 (0.2)	406	2770 (0.5)	408	3380 (2.0)
16.2091	H I 10–8	370	5.0 (0.7)	374	0.45 (0.0)	375	0.96 (0.1)	402	0.7 (0.02)	370	8.2 (0.5)	374	10(0.6)
16.8806	H I 12–9	389	2.3 (0.6)	409	0.24 (0.0)	262	0.59 (0.1)	405	0.3 (0.02)	404	2.7 (0.5)	381	5.7 (0.5)
17.0348	H_2 S(1)	407	2.0 (0.5)	394	0.48 (0.1)	399	1.5 (0.1)	399	1.2 (0.02)	398	6.1 (0.5)	397	9.9 (0.5)
17.8846	[P III]	396	4.3 (1.0)	416	0.71 (0.1)	421	0.99 (0.1)	427	1.8 (0.02)	404	12 (0.5)	403	16 (1.0)
17.9360	Fe II	392	7.1 (1.0)	376	0.76 (0.1)	378	0.93 (0.1)	398	0.9 (0.04)	391	13 (0.5)	394	15 (1.0)
18.7130	[S III]	382	609 (1.5)	382	54 (0.2)	388	160 (0.2)	396	129 (0.1)	382	1210 (1.0)	384	1560 (2.0)
18.7953	UIL	384	2.9 (1.5)	…	…	373	0.99 (0.2)	…	…	380	3.1 (1.0)	376	4.3 (3.0)
19.0619	H I 8–7	377	20 (1.5)	384	1.02 (0.1)	382	2.9 (0.2)	397	1.5 (0.02)	371	28 (1.0)	372	36 (4.0)
21.8302	[Ar III]	369	16 (3.0)	392	1.1 (0.8)	382	3.9 (0.7)	416	2.0 (0.1)	382	27 (2.0)	384	35 (2.0)
21.9600	UIL/He I	369	6.3 (0.7)	…	…	…	…	…	…	380	6.6 (2.0)	378	6.9 (2.0)
22.3404	H I 11–9/13–10	317	3.4 (0.7)	…	…	340	1.4 (0.4)	316	0.33 (0.1)	324	6.1 (2.0)	341	8.7 (2.0)
22.9250	[Fe III]	432	20 (0.7)	375	3.5 (0.5)	445	4.8 (0.4)	450	4.2 (0.1)	438	36 (2.0)	439	51 (2.0)
24.7470	UIL	…	…	…	…	…	…	380	1.1 (0.1)	…	…	…	…
25.2953	UIL	380	3.3 (1)	…	…	…	…	…	…	…	…	…	…
25.7340	[Ni IV]/UIL	…	…	…	…	…	…	380	2.4 (0.1)	…	…	…	…
25.8903	[O IV]	450	4 (2.0)	…	…	446	2.6 (0.2)	395	1.1 (0.1)	362	24 (3.0)	368	32 (5.0)
25.9884	[Fe II]	397	19 (2.0)	393	2.4 (0.2)	393	3.7 (0.2)	416	2.8 (0.1)	389	32 (3.0)	395	43(5.0)

Notes.
[a] Velocity centroids for lines are in kilometers per second.
[b] Units of flux are 10^{-18} W m^{-2}. Uncertainties in line fluxes are determined from fluxes in adjacent line-free continuum; see text. They do not include aperture correction or absolute flux calibration uncertainties. For lines much stronger than adjacent continuum, fluxes here are quoted to 1% but do not include the systematic ∼4% photometric uncertainty of MIRI/MRS.

D. P. Cohen et al. 2018). In addition to the bright core, there is a Brα source visible in adaptive-optics imaging that may be coincident with a faint radio continuum source about 0.″25 to the east of the supernebula core (D. P. Cohen et al. 2018); while these JWST/MIRI/MRS images do not have the spatial resolution to resolve this feature, it may be related to the bright optical source, Cluster 5 (D. Calzetti et al. 1997, 2015), directly south and east of the supernebula core. We do not see evidence in the MIR continuum that this is a separate cluster, although the petals of the PSF from D1 would complicate identification if a weaker source were present. It may simply be a denser part of the large-scale nebulosity emerging from the supernebula. The D1 region from which MRS spectra were extracted is defined here as a 0.″9 region, which is larger than the compact radio core.

While D1 is our primary target, regions D2, D4, and D6, although significantly less luminous, are also young massive clusters in their own right. D2 is associated with an optical and NIR point source and also coincides with a CO feature (S. M. Consiglio et al. 2017); a faint Hα point source is visible. D4 is notable because it has the strongest CO emission and most massive molecular cloud in the region (S. M. Consiglio et al. 2017), as well as embedded star formation. D4 is 50 times fainter in the continuum than source D1, but has a luminosity of $\sim 10^7\ L_\odot$, comparable to the giant H II regions W49 or 30 Doradus. Because D4 is $\lesssim 1''$ away (15 pc on the plane of the sky) from D1, it is affected by the spatial artifacts created by D1, including the PSF petals and the cruciform artifact. The D4 region is 0.″6 × 0.″7 in extent; it has the worst fringing of all the regions but also the strongest PAH features (Paper I). D4 will be a good case to study possible feedback effects from that very luminous cluster, although it is difficult to study with MIRI/MRS. D6 is a more diffuse region of radio continuum and CO emission region located ∼50 pc to the southwest of D1. Its H II region appears as a point-like Paα source (A. Alonso-Herrero et al. 2004); we associate D6 with Cluster 24 of J. Harris et al. (2004). Two additional regions were added. Chip corresponds to the 5 μm footprint, the smallest of the 12 spectral bands and the spatial region common to them all. Ellipse encompasses the plumes to the northwest and southeast of the central source apparent in the Hα image of Figure 1, and we henceforth refer to these Hα features as "the plumes." The D2 and D6 footprints overlap the edges of the 5 μm footprint, with sizes of 0.″8 and 0.″9, respectively. This is necessary to capture the extent of the longer wavelengths, whereas at 5–6 μm these sources appear to be well contained within the footprint.

3.1. Mid-infrared Emission Lines

In addition to strong continuum emission (J. L. Turner et al. 2026, Paper I), JWST/MIRI/MRS detected more than 70 ionic an molecular emission lines in the 5–25 μm spectra of NGC 5253. We have extracted line fluxes for each of the apertures corresponding to the four H II regions, D1, D2, D4, and D6, and the Ellipse and Chip (Figure 1). Line fluxes for the regions are presented in Table 1. The wealth of identified lines is due in part to the weakness of polycyclic aromatic hydrocarbon (PAH) features in this source. Velocity centroids determined from the Gaussian fits for the lines are also given and were used to verify the line identifications; lower-S/N lines can show a shift of 10–20 km s^{-1} within the MRS resolution of 80–200 km s^{-1}. The lines are for the most part

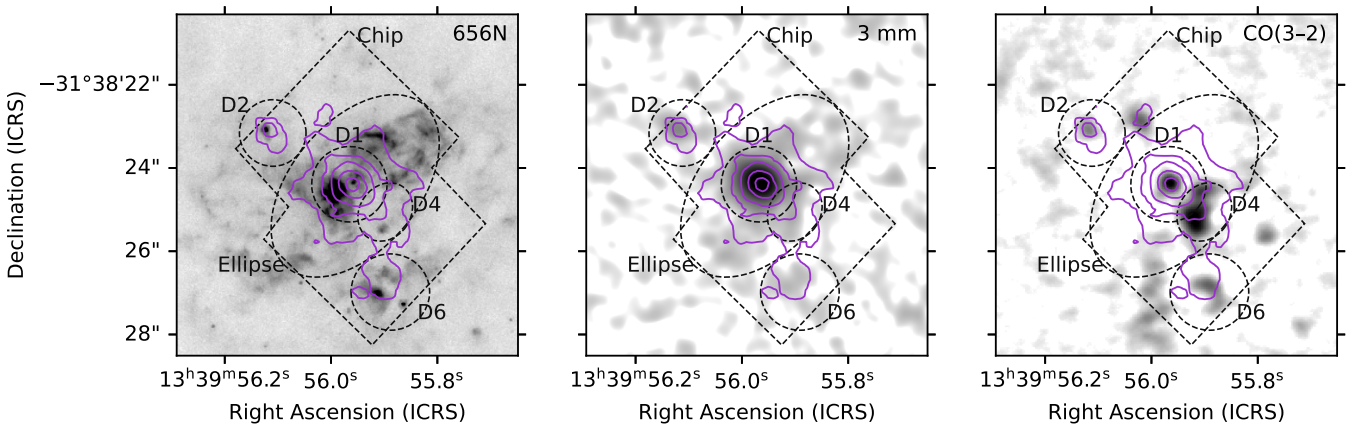


Figure 1. The JWST footprint (polygonal outline) and the regions used for spectral extraction are displayed as dashed circles and ellipses labeled D1, D2, D4, D6, Ellipse and Chip. They are overlaid on images of the source at Hα (HST image; D. Calzetti et al. 1997), 107 GHz (ALMA image, ALMA 203.1.00833; E. Rosolovsky), and the integrated flux of the ALMA CO(3–2) line (ALMA image; S. M. Consiglio et al. 2017; J. L. Turner et al. 2017). Color contours trace the 7 μm continuum emission from JWST/MIRI/MRS (J. L. Turner et al. 2026).

unresolved. Lines that have not yet been identified and are at wavelengths not consistent with any known ion at the velocity of NGC 5253 appear in the table as UnIdentified Line (UIL); unidentified absorption features are marked "UIA".

The full spectrum of the source D1 is displayed in detail in Figure 2. The 12 panels of the figure each show one wavelength band of the spectrometer, each on an intensity scale appropriate for that band. The figure illustrates the great richness of the infrared emission spectrum and the wealth of lines detected. Similar figures for the five other regions are included in the Appendix.

There are three types of emission lines detected: recombination lines of H I, fine-structure lines of metal ions, and the pure-rotational lines of H_2. Figure 3 displays each region's full spectrum in one panel, on log scales to display the strength of the main lines. It is apparent that the metal fine-structure lines and the strongest H I lines dominate the infrared emission. The H I recombination lines are produced in the ionized gas of H II regions. They have been extensively studied over the years and their behavior calculated for a very wide range of possible nebular conditions. There are 29 recombination lines of H I detected, from the Pfund ($n_L = 5$) and Humphreys ($n_L = 6$) series, as well as lines from the $n_L = 7$–10 series. In Section 4 we use the H I recombination lines to probe the ionization and stellar content of the sources, derive the total extinction, and find how the extinction depends on wavelength in the 5–25 μm range.

In Section 5 we introduce the fine-structure lines of metal ions. The emitting ions are photoionized, so their populations depend on the UV spectra of the exciting stars. These are magnetic quadrupole transitions and therefore "forbidden," and the emitting levels are collisionally excited, so these lines can be sensitive to the nebular density, as will be discussed below. The fine-structure lines are crucial for deriving the input ionization that excites the H II region emission.

We discuss briefly the basic picture the JWST data give of very high-excitation and hard-ionizing radiation in the starburst; full results from Cloudy and models of the exciting stellar populations will be presented in future papers, in which the rotational lines of H_2 will also be presented and discussed.

4. Extinction Law in the Mid-infrared

The NGC 5253 starburst is deeply embedded and obscured even in the MIR. The dominant star formation site in D1 is immersed within a CO cloud (J. L. Turner et al. 2017) and is so completely obscured at wavelengths shorter than 2.2 μm (A. Alonso-Herrero et al. 2004) that no stellar features are seen. Only the dusty compact H II region excited by the O stars is observable, and even that is only fully revealed at radio wavelengths (S. C. Beck et al. 1996; D. Calzetti et al. 1997). D2, D4, and D6 are also closely associated with molecular gas. We must therefore correct for the extinction if we are to understand the embedded stars.

The study of infrared extinction has until now largely concentrated on the *H*, *J*, and *K* bands, and has mostly depended on observing stars of known color index and spectral type on different sight lines through the interstellar medium (ISM). This method is limited in NGC 5253 because it requires sight lines to individual stars, which cannot be done here. Moreover, the sources in NGC 5253 appear to be so deeply embedded that they cannot be seen shortward of *J*. Using reddening to get extinction is also problematic: In NGC 5253, the Balmer line ratios suggest visual extinctions of $A_V \sim 1$–2 (J. R. Walsh & J.-R. Roy 1989; A. Monreal-Ibero et al. 2010), while the infrared recombination lines suggest that visual extinctions are at least $A_v \sim 15$ (J. L. Turner et al. 2003; A. Alonso-Herrero et al. 2004; N. L. Martín-Hernández et al. 2005). The only way to ensure a reliable extinction is to use an extinction-free measure of ionized gas, such as radio emission.

The JWST data make it possible to analyze the interstellar extinction over an unprecedented range of wavelengths, as well as to determine if and how it varies spatially over the starburst. We use the H I recombination lines of Table 2 to derive the extinction by comparing to radio free–free. NGC 5253 is a good site for this method because the solid-state features such as PAHs (J. L. Turner et al. 2026) are relatively weak, making it easier to detect the H I recombination lines. Table 2 shows the 32 recombination lines detected; they arise from five different series and cover the wavelength range from 4.9–22 μm. While some of these lines are weak, the suite of H I lines taken together allows us to determine both the total extinction and its variation with wavelength for the different regions. The technique is reviewed in the next section, 4.1, and the results for the individual regions presented in 4.2.

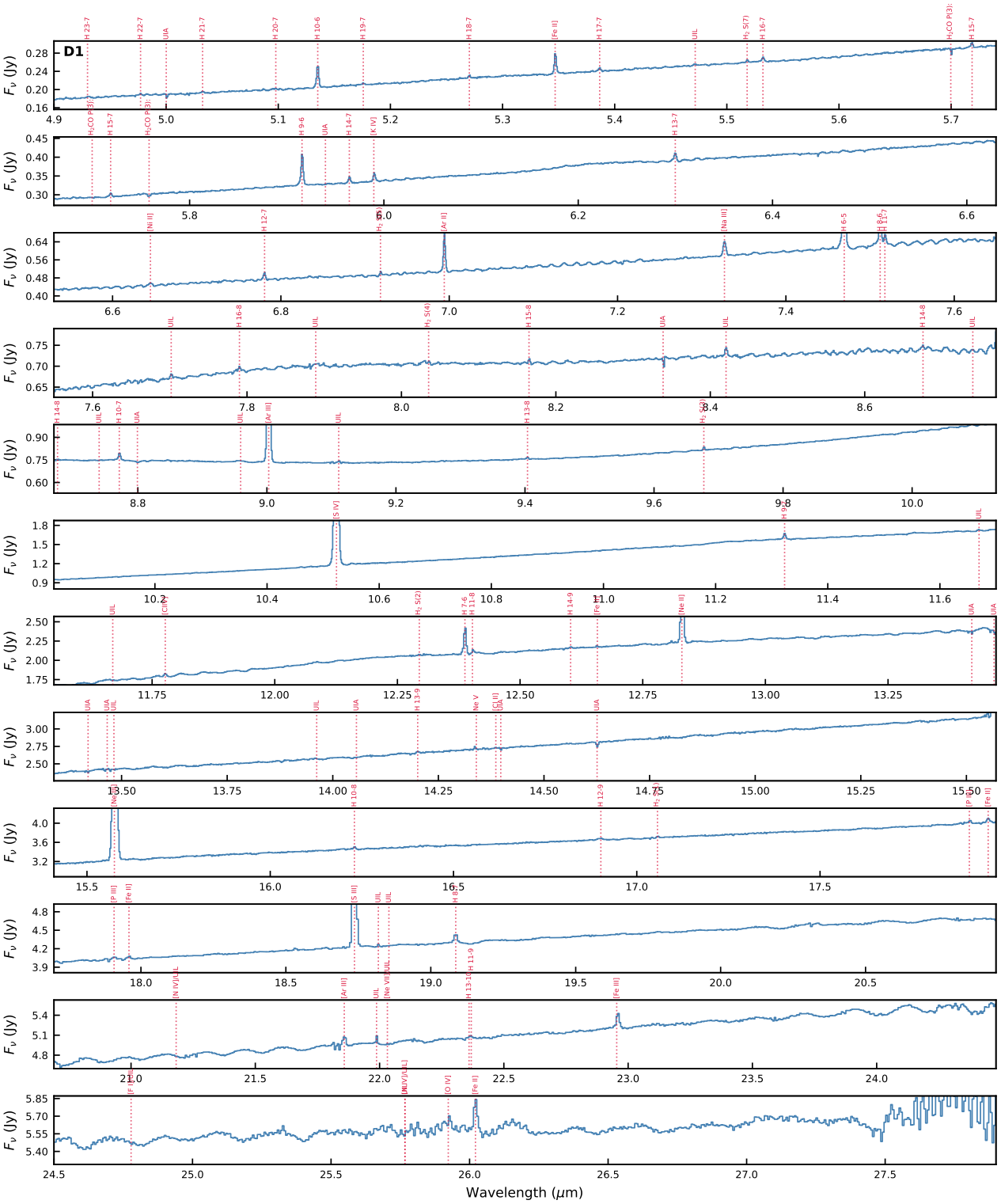


Figure 2. The full spectrum of the D1 region in a 0.″9 aperture. Expected line wavelengths are marked in red; not all lines are detected in all regions. Wavelengths are marked for a redshift of 380 km s^{-1}, the approximate radial velocity of the supernebula. Line fluxes are presented in Table 1. Small shifts of centroids from this wavelength may indicate gas motions within the region. Similar figures for the other regions are presented in the Appendix as Figures 10–14.

4.1. Calculating Extinction from H I lines and Radio Flux

We establish the interstellar extinction by comparing the H I recombination lines in the JWST spectra to the millimeter-wave free–free emission, which is unaffected by extinction. Simple H II regions have free–free emission that is optically thick ($\propto\nu^{-2}$) at low frequencies and transitions to optically thin ($\propto\nu^{-0.1}$) at a turnover frequency determined by the emission measure, EM $= \int n_e^2\, d\ell$. For moderate (EM $\sim 10^4$ cm^{-6} pc) emission measures, typical of evolved H II regions, the emission becomes thin at frequencies higher than $\sim$1 GHz ($\lambda = 20$ cm). The emission measure in D1 is high, (EM $\gtrsim 10^8$ cm^{-6} pc; S. C. Beck et al. 1996; J. L. Turner & S. C. Beck 2004), and the overall

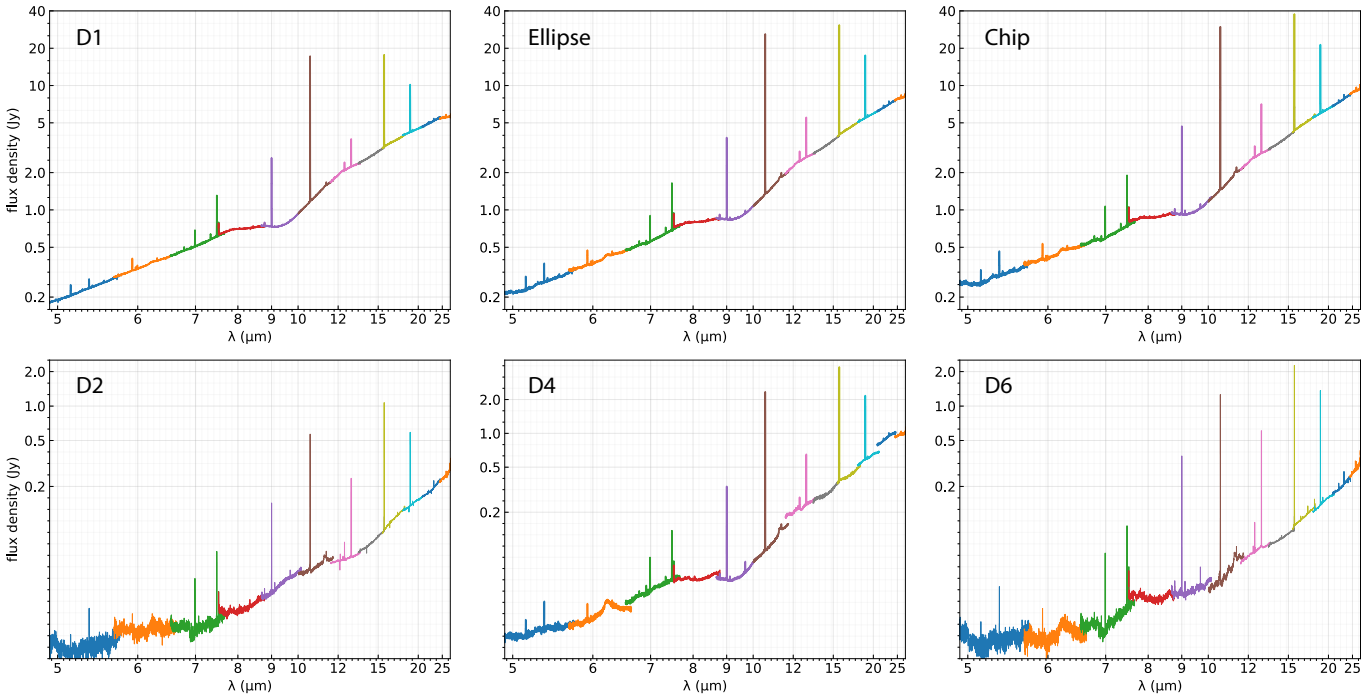


Figure 3. Spectra of the individual regions. The x-axis is log-scaled and the y-axis scaled as frequency; the tick units are as shown. D1, Ellipse, and Chip are plotted to the same scale, as are D2 and D6.

spectrum of D1 suggests that it is optically thin only at frequencies beyond ∼15–20 GHz (∼1 cm; D. S. Meier et al. 2002; J. L. Turner & S. C. Beck 2004; C. A. Rodríguez-Rico et al. 2007).

We rely on ALMA maps at 1.3 and 3.0 mm (ALMA Project 2016.1.00829, PI: D. S. Meier; ALMA Project 2013.1.00833.S, PI: E. Rosolovsky) for our derivation of $N_{\rm lyc}$ for the regions. At millimeter wavelengths, nonthermal radiation is negligible. Comparison with ALMA 345 GHz maps indicates that the 1.3 mm flux is entirely optically thin free–free emission, except possibly in D4; at 3 mm the emission is pure free–free in all regions. For an ionization-bounded nebula, the free–free flux is directly related to $N_{\rm lyc}$. The millimeter beams are smaller than our MIRI spectral aperture sizes, and the largest angular scale detected by the interferometer is larger than the MIRI/MRS footprint. Since the JWST cubes were aligned to high-resolution 1.3 mm ALMA images (Section 2; J. L. Turner et al. 2026), we use the same WCS regions for both radio and infrared flux measurements.

The strength of an H I recombination line and of the thermal radio (free–free) continuum are linked. Integrated over the volume of an H II region, they both depend on the Lyman continuum flux, $N_{\rm lyc}$. For an ionization-bounded, pure H nebula and Case B recombination, the flux of an emission line between the upper and lower levels, u, l, is given by

$$\frac{S_{\rm line}}{\rm erg\ s^{-1}\,cm^{-2}} = 8.33 \times 10^{-51} \frac{N_{\rm lyc}}{D^2_{\rm Mpc}} \left(\frac{\varepsilon(u \rightarrow l)}{\alpha_B} \right),$$

where $\varepsilon(u \rightarrow l)$ is the emissivity and α_B the Case B recombination coefficient, with line emissivities from P. J. Storey & D. G. Hummer (1995). The thermal radio emission S_ν depends on $N_{\rm lyc}$ as

$$\left(\frac{S_{100}}{\rm mJy} \right) = 7.604 \times 10^{-51}\, T_4^{0.507}\, \nu_{11}^{-0.118} \left(\frac{n_p}{n_e} \right) D^{-2}_{\rm Mpc} \left(\frac{N_{\rm lyc}}{s^{-1}} \right),$$

where T_4 is the temperature in units of 10^4 K, and ν_{11} is the frequency in units of 100 GHz. The temperature and frequency dependence in the formula for the radio emission arise from the Gaunt factor in the expression for free–free τ and the temperature dependence of α_B (B. T. Draine 2011a, 2011b). For $T = 10^4$ K, the ratio of line to free–free flux simplifies to $(S_{\rm line}/10^{-18}\,{\rm W\,m^{-2}}) = 0.429\,{\rm em}_{28}\,S_{100{\rm GHz}}({\rm mJy})$, where ${\rm em}_{28}$ is the emissivity in units of $10^{-28}\,{\rm erg\,s^{-2}\,cm^{-3}}$. The line emissivities depend on temperature as $T_4^{-1.2}$ for infrared lines and are relatively insensitive to density. Optical spectroscopy of NGC 5253 (J. R. Walsh & J.-R. Roy 1989; H. A. Kobulnicky et al. 1997; Á. R. López-Sánchez et al. 2007; A. Monreal-Ibero et al. 2012; B. G. A. Pruijt et al. 2026) indicates temperatures of 9700–12,100K. We adopt $T_e = 10^4$ K, within the range of computed T_e (N. G. Guseva et al. 2011). Considering that the free–free and recombination lines tend to arise in gas that is slightly cooler than the forbidden lines, we estimate that the uncertainty due to temperature in the ratio is $\lesssim$3%–4%. Table 2 gives the $\varepsilon(u \rightarrow l)$ for the H I lines in the JWST dataset.

Table 2 gives the H I line fluxes for all lines detected at the 2σ level or stronger for each of the D1, D2, D4, and D6 sources and for the Ellipse and Chip regions. The radio flux for each region is listed in Table 2, as are the emissivities for reference temperature $T_e = 10^4$ K and electron density $n_e = 10^4\,{\rm cm^{-3}}$ for each line. We compute the extinction from the observed line strength to that predicted by the radio emission using the equation given.

Table 2
H I Line Fluxes in NGC 5253

Line	λ (μm)	$em_{28}(u \rightarrow l)$[a]	Line Flux D1	D2	D4	D6	Ellipse	Chip
					(10^{-18} W m^{-2})			
H I 23–7	4.9237	0.214	1.4 ± 0.2	…	…	…	2.5	…
H I 22–7	4.9709	0.281	1.1 ± 0.2	…	…	…	0.97 ± 1.0	1.4
H I 21–7	5.0261	0.244	1.2 ± 0.3	…	0.28 ± 0.3	1.9 ± 1.0	2.1 ± 1.0	1.6
H I 10–6 (Huδ)	5.1287	4.10	14 ± 0.1	0.96 ± 0.1	1.7 ± 0.2	1.8 ± 0.1	19 ± 0.7	22 ± 1.0
H I 19–7	5.1693	0.382	1.2 ± 0.1	…	…	…	1.4 ± 0.7	2.2 ± 1.0
H I 18–7	5.2637	0.452	1.1 ± 0.2	…	0.5 ± 0.1	…	2.4 ± 0.7	2.9 ± 1.0
H I 17–7	5.3798	0.539	1.7 ± 0.3	…	…	…	4.2 ± 0.7	4.3 ± 1.0
H I 16–7	5.5252	0.649	2.4 ± 0.3	…	…	…	4.2 ± 0.7	4.7 ± 0.7
H I 15–7	5.7115	0.792	2.6 ± 0.2	…	…	1.0 ± 0.4	4.5 ± 0.5	6.3 ± 1.0
H I 9–6 (Huγ)	5.9082	5.66	21 ± 0.2	1.0 ± 0.1	2.2 ± 0.2	1.5 ± 0.1	30 ± 0.5	34 ± 0.5
H I 14–7	5.9568	0.979	3.5 ± 0.2	…	0.22 ± 0.3	…	5.2 ± 0.5	6.3 ± 0.5
H I 13–7	6.2919	1.23	5.1 ± 0.8	…	0.67 ± 0.1	0.7 ± 0.1	7.7 ± 0.5	8.1 ± 1.0
H I 12–7	6.7720	1.57	5.6 ± 0.1	0.35 ± 0.1	0.60 ± 0.2	0.6 ± 0.2	7.9 ± 0.3	10 ± 1.0
H I 6–5 (Pfα)	7.4599	30.4	118 ± 0.5	6.7 ± 0.1	13 ± 0.4	10.6 ± 0.1	160 ± 1.0	189 ± 0.6
H I 8–6 (Huβ)	7.5025	8.06	33 ± 0.5	1.7 ± 0.1	3.5 ± 0.4	3.1 ± 0.1	42 ± 1.0	51 ± 0.6
H I 11–7	7.5081	2.05	8.8 ± 0.5	0.44 ± 0.1	0.92 ± 0.4	0.8 ± 0.1	11 ± 1.0	13 ± 0.6
H I 15–8	8.1549	0.555	1.1 ± 0.3	…	…	0.4 ± 0.1	1.9 ± 0.5	2.9 ± 0.4
H I 14–8	8.6645	0.686	…	…	…	…	2.2 ± 1	…
H I 10–7	8.7601	2.73	7.3 ± 0.3	0.52 ± 0.1	0.7 ± 0.1	0.7 ± 0.1	11 ± 0.7	14 ± 0.7
H I 13–8	9.3920	0.860	1.2 ± 0.2	…	0.16 ± 0.1	…	1.9 ± 0.4	2.0 ± 0.6
H I 16–9	10.8036	…	…	…	…	…	…	0.5 ± 0.3
H I 9–7	11.3087	3.71	11 ± 0.4	0.75 ± 0.2	1.2 ± 0.1	0.9 ± 0.1	16 ± 2.0	20 ± 0.3
H I 15–9	11.5395	…	1.7 ± 0.2	…	…	…	1.5 ± 0.3	2.0 ± 0.3
H I 7–6 (Huα)	12.3719	11.5	39 ± 0.2	2.2 ± 0.0	6.7 ± 0.3	4.0 ± 0.1	61 ± 1.5	76 ± 0.6
H I 11–8	12.3872	1.42	5.1 ± 0.2	0.27 ± 0.0	0.91 ± 0.3	0.4 ± 0.1	4.9 ± 1.5	11 ± 0.6
H I 14–9	12.5871	0.497	1.7 ± 0.4	…	…	…	2.0 ± 0.3	2.8 ± 0.6
H I 13–9	14.1830	0.621	2.1 ± 0.2	…	…	0.2 ± 0.1	3.0 ± 0.3	4.8 ± 0.3
H I 10–8	16.2091	1.86	5.0 ± 0.7	0.45 ± 0.0	0.96 ± 0.1	0.7 ± 0.02	8.2 ± 0.5	10 ± 0.6
H I 12–9	16.8806	0.785	2.3 ± 0.6	0.24 ± 0.0	0.59 ± 0.1	0.3 ± 0.02	2.7 ± 0.5	5.7 ± 0.5
H I 8–7	19.0619	4.98	20 ± 1.5	1.02 ± 0.1	2.9 ± 0.2	1.5 ± 0.02	28 ± 1.0	36 ± 4.0
H I 11–9	22.3404	1.00	3.4 ± 0.7	…	1.4 ± 0.4	0.33 ± 0.1	6.1 ± 2.0	8.7 ± 2.0
Free–free[b]	2.8mm		27.6 ± 0.27	0.83 ± . 08	1.3 ± 0.1	0.8 ± 0.08	30.5 ± 0.31	32.1 ± . 032

Notes.
[a] Emissivities are from P. J. Storey & D. G. Hummer (1995), with units (10^{-28} erg s^{-1} cm^3).
[b] Free–free fluxes are in units of mJy. The uncertainties in line fluxes in the table are statistical uncertainties due to the Gaussian fits to the lines. Absolute flux uncertainties are dominated by absolute photometric accuracy, apertures, and astrometry, estimated to be ∼10%. Uncertainty in the free–free fluxes is the standard photometric uncertainty for this ALMA band.

We take the uncertainties in the line strengths from Table 2, and for the ALMA measurements, adopt the standard photometric accuracy of 5% (I. Argyriou et al. 2023a). The formal errors in the MIR line fluxes based on the Gaussian fits are in many cases much less than the systematic uncertainties that dominate much of the spectrum. While the photometric accuracy and reproducibility of the system is estimated to be 2%–6% (I. Argyriou et al. 2023a; D. R. Law et al. 2023), uncertainties in the baselines assumed for the line fits are generally larger and difficult to characterize. Fringing can vary both spatially and spectrally; while the spectra have been defringed, fringes are still present and can affect the baseline, although this should wash out statistically for many lines. There is also the presence of weak PAH emission, which affects mostly the H I 9–7 line at 11.3 μm. Fringing, instrumental response, and baseline effects, which are related, are likely to dominate the uncertainties in the line fluxes, in different proportions for each line.

Because the uncertainties in the MRS line fluxes are driven by continuum variations such as fringing or PAHs, the fluxes are in large part independent from line to line. Thus we can use the ensemble of lines to fit the extinction across the band, assuming that it varies relatively smoothly. We do a least-squares fit to a linear model for the variation of apparent extinction, $A(\lambda) = a + b\lambda$. Points above a S/N of 10 were assigned a weight of 1; although the formal S/N of the line fluxes in a relative sense may be higher than 10, we are doing a ratio of JWST and ALMA fluxes and therefore must sum their absolute photometric accuracies, which we estimate at ∼5% each. Points below S/N = 10 were weighted as $1/(S/N)^2$. We redid the fits with uniform weighting, and the results were indistinguishable.

In Figure 4 we show the apparent extinction, derived from the observed and radio-predicted fluxes, as $A^{app} = -2.5\log(S^{obs}/S^{pred})$, for each point. The best-fit linear model is shown. The plots show that the MIR extinction for all the NGC 5253 sources is flat with wavelength, as is the case in the Galaxy (K. D. Gordon et al. 2023) and other galaxies (e.g., T. S. Y. Lai et al. 2024; T. S. Y. Lai et al. 2025). D1 has a small positive slope of 0.02 ± . 008 at the 95% confidence level; for all other regions the fitted slopes are consistent with zero.

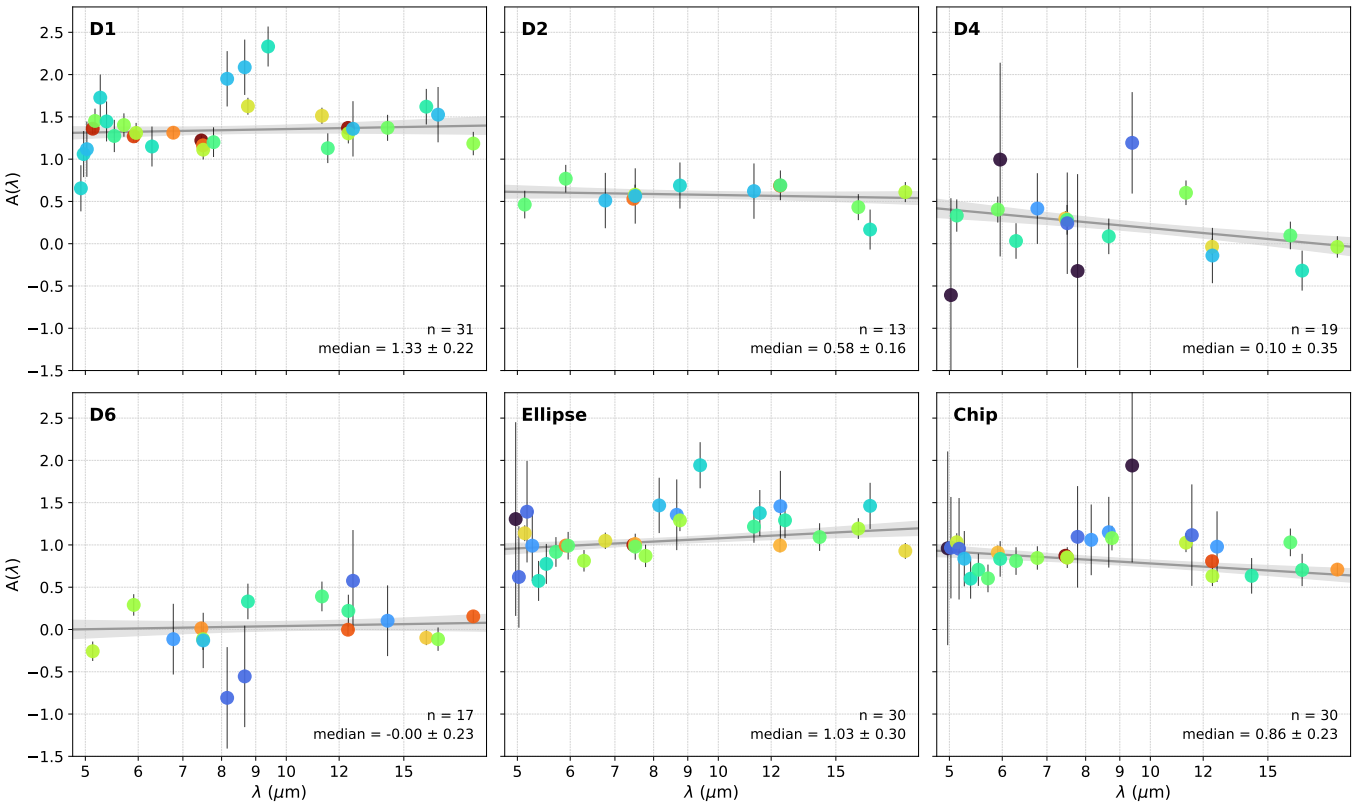


Figure 4. Apparent extinction in each region as determined by the comparison of observed H I line flux to that predicted from millimeter-wave free–free fluxes. On the lower right of each panel we give the number of H I lines observed in that region and the median derived extinction. Error bars for fluxes are shown on each point, and are also color-coded on a log scale with the highest S/N in red, through yellow to green to blue to the lowest S/N in black. The best-fit linear regression is shown with 95% confidence levels for predictions. The higher error and lower S/N around 9–10 μm in D1, Ellipse, and Chip are caused by PAH features and silicate absorption (J. L. Turner et al. 2026).

Since the extinction is flat, each region can be characterized by a single value for the extinction over the 5.9 μm to 19.1 μm range as A(5–19 μm) or A(MIR). The median value for each region is shown in the figure. D1 has the highest extinction across the wavelength range, A(MIR) $= 1.3 \pm 0.2$; of the regions that include D1, Ellipse has A(MIR) $= 1.0 \pm 0.3$ and Chip has A(MIR) $= 0.86 \pm 0.23$. D2 has a lower extinction of A(MIR) $= 0.58 \pm 0.2$. D4 and D6 are consistent with zero MIR extinction, with A(MIR) $= 0.1 \pm 0.35$ for D4 and A(MIR) $= 0.0 \pm 0.23$ for D6. D4 has the greatest scatter of $\sim$0.4 mag, probably due to its proximity to D1 and its location near the cruciform feature and its strong fringing.

It is notable that the Ellipse and Chip regions, in which the flux is dominated by D1, have lower extinction than does D1. The apparent extinction or attenuation, $A^{\rm app} = -2.5\log(S^{\rm obs}/S^{\rm pred})$, is a lower limit to the "mean" extinction across the source (A. Natta & N. Panagia 1984). While the regions other than D1 have <15% of the total radio flux, they constitute 30% of the observed MIR flux. NGC 5253 is nearby, and we can isolate individual H II regions on 15 pc scales; for more distant galaxies, where this is not possible, the effect is enhanced. For NGC 5253, the standard correction for "mixed" extinction overestimates the correction for this relatively simple region consisting of four H II regions combined within the MIRI/MRS footprint.

For region D1, we can extend the analysis of extinction into the NIR by adopting fluxes for H I lines found from other high-resolution observations. The HST/NICMOS observations of A. Alonso-Herrero et al. (2004) and the Keck/NICMOS observations of J. L. Turner et al. (2003), although slit spectra, have sufficient spatial resolution to isolate D1. Those results, combined with the present findings, are plotted in Figure 5 and show a steep fall-off from the NIR.

How do these values for extinction compare to other results, and what do they say about the starburst environment of NGC 5253? Extensive work in the J, K, and L bands over the years (e.g., M. J. Lebofsky & G. H. Rieke 1979; K. D. Gordon et al. 2021; M. Decleir et al. 2022) has demonstrated that extinction $A(\lambda)$ falls steeply with λ from the visible to $\lambda \sim 4$ μm and can be approximated as λ^{-k} for k typically between 1 and 2. For example, the extinction to the Galactic center, derived like our work from H I recombination lines (D. Lutz et al. 1998), falls as $\approx\lambda^{-1.75}$ from the visible to $\sim$4 μm wavelength. At $\sim$4 μm it flattens out to be near constant as λ increases until the silicate feature at 9.7 μm (R. Indebetouw et al. 2005; K. D. Gordon et al. 2021). The current results, combined with the Brackett line results of J. L. Turner et al. (2003) and A. Alonso-Herrero et al. (2004), show the same behavior: There is significant relative extinction between Brγ at 2.17 μm and Brα at 4.05 μm, while the ratios of Brα 4.05 μm and Pfα 7.46 μm are closer to the theoretical ratio predicted from the radio.

There is less known in other sources for the behavior of extinction at wavelengths longer than $\sim$12 μm, but the situation is rapidly changing with JWST. Previous studies find the extinction in the MIR is consistent with flat out through the 19 μm H I line, excluding the 9.7 μm and 18 μm silicate features (D. Lutz et al. 1996; J. E. Chiar & A. G. G. M. Tielens 2006; J. D. T. Smith et al. 2007; K. D. Gordon et al. 2021, 2023). The NGC 5253 result is

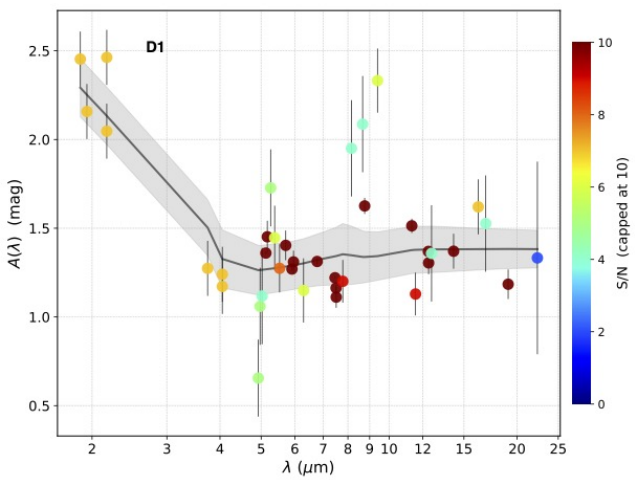


Figure 5. Apparent extinction to D1 over NIR to MIR wavelengths, determined by the comparison of observed flux to flux predicted from 107 GHz free–free flux, and including data for $\lambda < 5\mu$m from Keck and HST (J. L. Turner et al. 2003; A. Alonso-Herrero et al. 2004), as well as JWST/MIRI/MRS fluxes. Error bars are shown on each point and S/N is color-coded as shown by the wedge. A loess-smoothed fit from R (span 75%) with 95% confidence levels for predictions is shown. The lines around 5 μm are from weaker high-level lines of the n-7 series, which have large scatter due to the instrumental response at the band edge (see Paper I) and the presence of PAH emission. The high values around 9–10 μm show the influence of the silicate absorption in D1, discussed in the text.

consistent with the flat extinction curve seen in higher-metallicity systems, and has the advantage of being based on the ratio of multiple H I lines to extinction-free radio emission.

Finding that the extinction is near constant through the JWST wavelength range has the immediate consequence that ratios formed of two lines in this range will be insensitive to extinction, with the exception of the [Ar III] line, which is affected by silicate absorption, as noted later. This will be important as we sketch out the nebular conditions in the following sections of this paper.

4.2. Extinction to the Individual Regions

D1 completely dominates the ionization, providing more than 80% of the $N_{\rm lyc}$ in the Chip aperture. Its 1.3 mag of MIR extinction is higher than any other region in the field and is high by any standard, being close to the total extinction to the Galactic center in the Milky Way. D. Calzetti et al. (1997) determined a visual extinction of A_V = 9–35 mag from comparing the observed Hα flux to that predicted by the 2 cm free–free fluxes of S. C. Beck et al. (1996). The recent extinction curves of K. D. Gordon et al. (2023) give $A(14\,\mu{\rm m})/A_V = 0.04$, which with our MIR extinction value to D1 gives $A_{\rm V} = 33$ mag, in agreement with the upper bound of D. Calzetti et al. (1997).

Inferring gas columns for D1 from this number is difficult for such a large extinction. The supernebula core is embedded/mixed with a very bright CO(3–2) source (J. L. Turner et al. 2015, 2017). Unusual conditions such as apparently optically thin CO (S. M. Consiglio et al. 2017) and high CO temperatures lead to uncertainty in the molecular gas mass of more than an order of magnitude (J. L. Turner et al. 2017). It is difficult to infer much about dust or gas columns with current information. It is clear, however, that while line ratios within the MIR are unaffected by reddening, there is still an attenuation of fluxes even in the MIR.

D2 appears in every respect to be a young and obscured young stellar cluster: It appears as a discrete source in radio maps at 15, 33, 107, and 230 GHz, is a CO(3–2) and 870 μm continuum source, and has a weak counterpart in the optical Hα (Figure 1). We find A(MIR) = 0.58 mag for D2, implying a visual extinction of $A_V \sim 15$ mag. D2 has a very substantial ionization rate of $1.2 \times 10^{51}\,{\rm s}^{-1}$ from the radio flux; at $L \sim 10^7\,L_\odot$, it is comparable to the brightest star formation regions in the Milky Way. Although it has lower extinction than D1, it still falls into the category of "embedded" young clusters with significant MIR extinction. D2 has visible Hα emission, albeit a tiny fraction of what is expected based on its radio luminosity. For these photons to have escaped argues that the extinction in D2, like D1, has a clumpy or porous internal structure.

D4 and D6 are difficult to interpret. Both of them have much lower obscuration than D2 and D1, with infrared extinction formally close to A(MIR) $\sim$ 0; given the uncertainties, they could have extinctions as high as $A_V \sim 5$ mag. D4 is so close (15 pc) to the dominant D1 cluster as to nearly overlap it in the JWST PSF, and it is particularly affected by the cruciform feature. D4 is a very intriguing source; it has some of the strongest CO emission in the field (Figure 1), as well as the strongest PAH emission (J. L. Turner et al. 2026, Paper I). Therefore, it is surprising that the extinction is lower than that of D1 or D2. It may be a blister feature or irradiated by the nearby D1 cluster, or some of the MIR H I flux could be spilling over from D1. D6 is a CO(3–2) and 870 μm source associated with [Ne III] and some Hα optical emission. Its radio continuum emission is diffuse, although consistent with a very luminous ($L \sim 10^7\,L_\odot$) star-forming region. The extended and irregular shape of the molecular and continuum emission suggest a fragmentary cloud or filament. It appears to coincide with J. Harris et al.'s (2004) cluster 24.

4.3. The Silicate Feature in NGC 5253 Does Not Correlate Simply with the Extinction

In Galactic H II regions, as well as in many highly luminous starburst, active galactic nucleus (AGN), and hybrid galaxies, the MIR spectrum has strong absorption features at 9.7 and 18μm, which are attributed to the stretch and bending modes of silicates. These features are detected in the JWST data for the first time in NGC 5253, as shown in the continuum spectra in Figure 3. In Paper I, we fit the 9.7 μm feature in the observed sources following the method of H. W. W. Spoon et al. (2007), and find $\tau_{9.7} = 0.3 \pm 0.1$ in D1. D4 also shows the silicate feature in absorption, weaker than D1 and probably affected by it.

The 9.7 μm feature is important as its strength has been observed to correlate with the total obscuration. D. C. B. Whittet (1992) found $A_v/\tau_{9.7} = 18.4 \pm 1$ for many Galactic sources (but not all; the ratio is low in the Galactic center; D. C. B. Whittet 1992; K. D. Gordon et al. 2021). In NGC 5253, the silicate features are strikingly *weak* for the amount of obscuration. D1 has $A_v/\tau_{9.7} \sim 100 \pm 20$, 5 times higher than the Galactic value. D6 lacks silicate absorption, which is consistent with its lower MIR extinction.

The 9.7 μm silicate feature appears in emission in D2. Silicate emission is present in asymptotic giant branch (AGB) stars and its appearance here may argue that star formation is more evolved in D2 than D1. Silicates are also observed in emission toward the Trapezium (D. Cesarsky et al. 2000) and

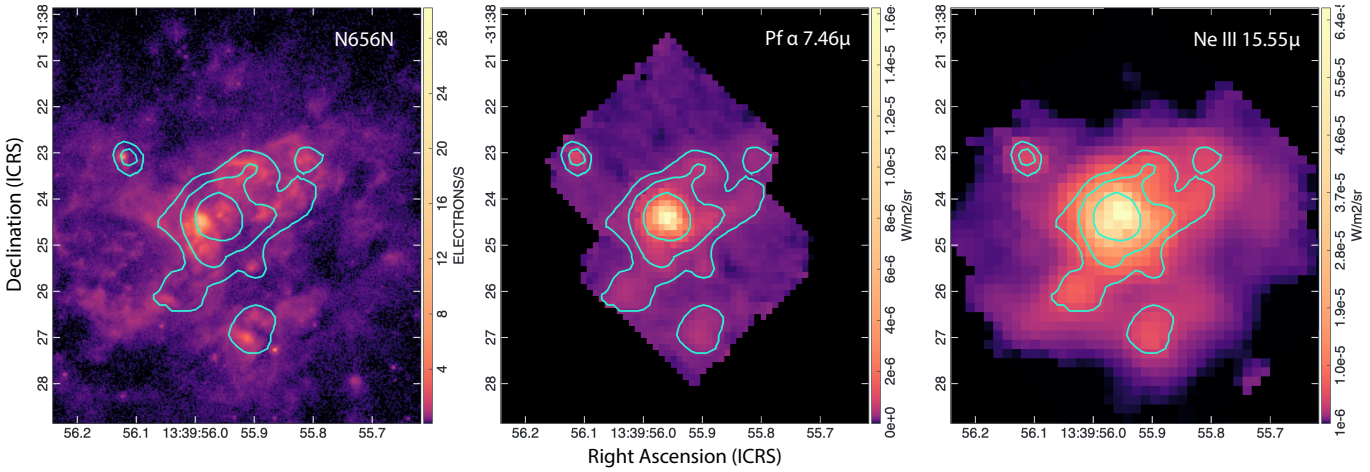


Figure 6. Emission from the giant H II region, NGC 5253-D1, and its environs. Contours in each panel are of Pfα emission at values of (2, 4, 16) $\times 10^{-6}$ W m^{-2} sr^{-1}. Left: HST 656N image, Hα. Middle: MRS continuum-free line map of Pfα, H I 6–5. Right: MRS continuum-free line map of [Ne III].

source N66 in the LMC (D. G. Whelan et al. 2013), where they are attributed to hot dust lying on the near side of the source.

5. Fine-structure Lines and Nebular Conditions in the NGC 5253 Starburst

Figure 3 shows the spectra of the sources, displayed on log scales so the full strength of the lines is apparent. Especially important in the MIR are the lines of argon, sulfur, and neon: Each element has lines from two different ionization states in this spectral range. The relative strength of the lines depends on the relative abundances of the ions and thus on the hardness of the ionizing spectrum. It is immediately apparent from Figure 3 that the NGC 5253 spectra are dominated by lines of the higher ionization species: [Ne III] 15.5 μm (41 eV) and [S IV] 10.5 μm (35 eV) are the strongest lines in every source, while [Ne II] 12.8 μm (22 eV) and [S III] 18.7 μm (23 eV) are far weaker. [Ar III] 8.99 μm (28eV) is clearly stronger than [Ar II] 6.99 μm (16eV) in every spectrum.

We can compare the MIRI/MRS fluxes to previous Infrared Space Observatory (ISO) and Spitzer measurements with larger apertures. A. Verma et al. (2003) examined the ISO measurements of MIR emission lines in a dozen starburst galaxies, including NGC 5253. P. Beirão et al. (2006) presented the Spitzer observations of NGC 5253. The fluxes are generally consistent given that both the ISO and Spitzer apertures are much larger. We compare our fluxes for the Chip region to the Spitzer fluxes, and we find that JWST detects 68%–72% of the [Ne II] and [Ne III] line fluxes detected by Spitzer and 90%–98% for the [S III] and [S IV] lines. Thus the JWST chip seems to pick up nearly all of the sulfur emission in the central $11'' \times 5''$ Spitzer aperture, but only two-thirds of the neon emission, and only one-third of the Huα. These are strong lines with high S/N; even including systematic uncertainties, these differences are significant and suggest that the lines have distinct spatial distributions. With the high spatial resolution of MIRI/MRS, we can investigate these differences.

5.1. Spatial Distribution of the Fine-structure Lines

Fine-structure lines of metal ions are the dominant MIR emission lines in H II regions, among the main coolants of the nebulae, and excellent probes of nebular conditions. The JWST spectra of NGC 5253 include lines of neon, argon, sulfur, and some as yet unidentified features.

Figure 6 shows the distribution of the [Ne III] 15.5 μm line over the JWST field. Comparison to the 656N and Pfα images shows that the [Ne III] line emission tracks perfectly with the Pfα. Prominent plumes of Hα emission with a full extent of $\sim$100 pc, which also appear in the JWST/MIRI/MRS Pfα image, suggest a common origin near the central radio source. The origin of the plumes is not clear; are they excited by the deeply embedded radio supernebula core, or by an active ambient radiation field? The high ionization state of the plumes (shown by the [Ne III] emission) suggests that they may be excited by D1 photons that have escaped the high extinction around that source, since the D1 cluster is sufficiently luminous to contain a significant number of the very massive stars producing these energetic photons. D2 and D6, luminous H II regions themselves, are more localized sources of [Ne III].

Figure 7 displays the integrated line emission of each of the main fine-structure lines. These images were generated by subtracting a median-averaged continuum from an image of the peak pixel in the wavelength range of the line, a "MOM8" image. For these high-dynamic-range and spectrally unresolved lines, the MOM8 image is proportional to the integrated line intensity. D1 dominates in every line, and D2 and D6 appear as distinct sources. There are definite qualitative differences in spatial distribution between the lower-excitation ([Ar II], [S III], and [Ne II]) and higher-excitation ([Ar III], [S IV], and [Ne III]) lines. The high-excitation ions are generally more concentrated in compact structures such as the H II regions while the low-excitation ions are more extended. South and west of D1, in particular, the low-excitation [S III] and [Ar II] fill in almost the entire chip area. Another difference is the extended emission north and west of D1, the northern "plume" feature, that appears in all the maps, but most clearly in the high-excitation ions. This component of gas also appears in the radio and Hα maps as part of the plumes.

These features are on too small spatial scales to be seen in the ISO or Spitzer data. The highest-spatial-resolution measurements in the literature for any of these ions are Gemini/TEXES observations of [S IV] by S. C. Beck et al. (2020) with a 0.″3 beam. Those maps show gas extending west and northwest of D1, which S. C. Beck et al. (2020) called

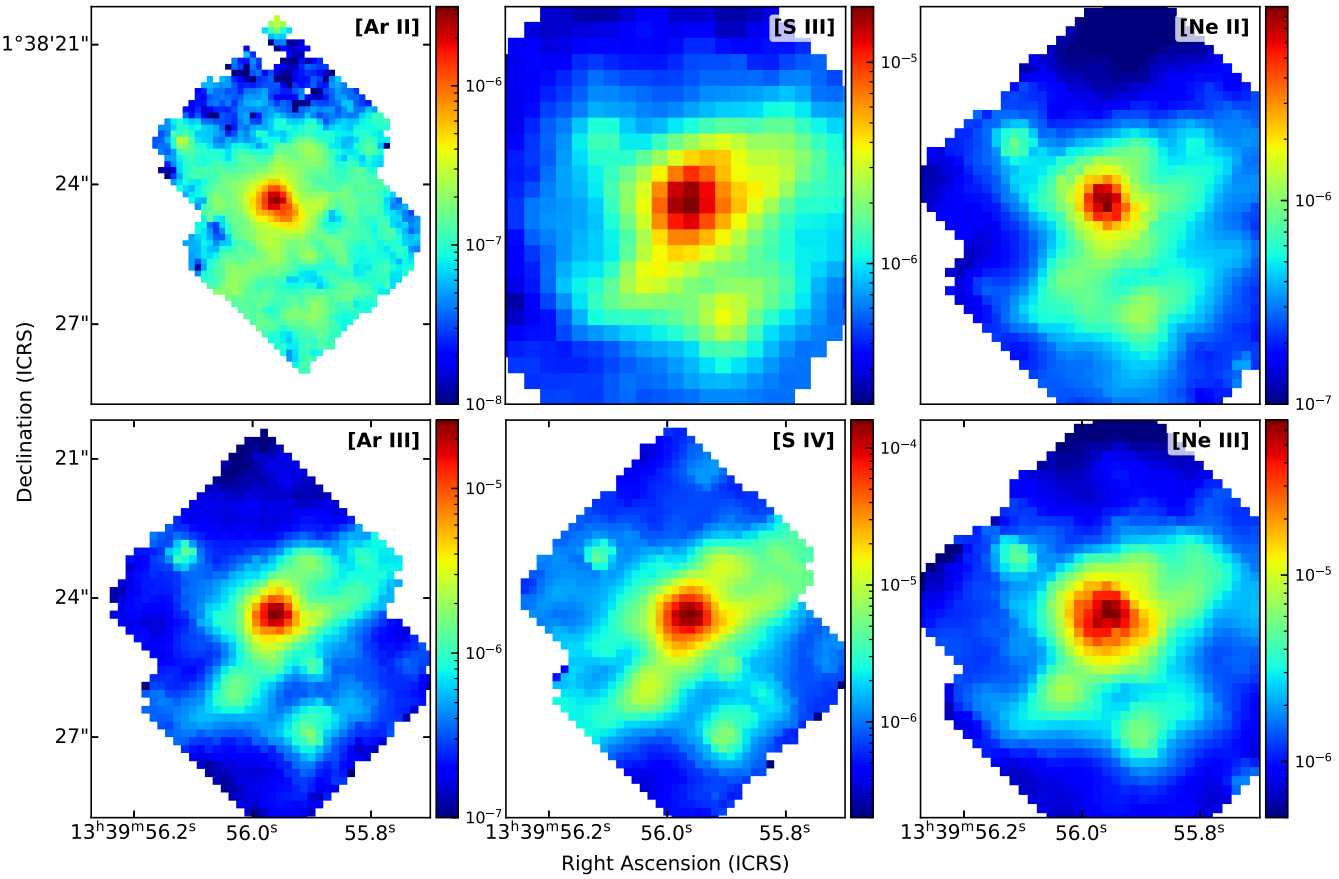


Figure 7. Continuum-subtracted integrated line intensity (MOM0) maps of the important fine-structure lines in the MRS spectra. Color bars give intensities in W m^{-2} sr^{-1}.

"arms." These arms agree in position and angle with the base of the structure, which appears as an elongated "loop" in the current ionic line maps and in the radio continuum of Figure 1, and with a plume appearance in the Hα images. The Gemini/TEXES observations did not have the dynamic range to see the full extent of this structure, only the strongest emission close to D1. The TEXES spectra have the advantage of a high spectral resolution of 4 km s^{-1}, and show that gas in this western area is blueshifted by about 30 km s^{-1} relative to D1. This suggests strongly that the loop is kinematically distinct from the main source and may be an outflow or an expanding ring. This has also been suggested by lower-resolution observations (M. S. Westmoquette et al. 2013).

Another feature seen in the Gemini/TEXES maps is a distinct source at R.A. 13:39:56.054, decl. –31:38:25.64. This source also appears in the radio continuum and in the high-excitation-ion maps as an emission clump SE of D1, although it can unfortunately be confused in the JWST maps by the petal artifact. This clump is kinematically distinct, with an [S IV] line at the same velocity at D1 but with only about half the FWHM. It may be another outflow, but its nature is not yet clear.

Keck/NIRSPAO adaptive-optics Brα and He I slit spectra of D. P. Cohen et al. (2018) see a velocity shift of 13 km s^{-1} across the inner 1.″2 core of the supernebula, which they suggest might be due to a bipolar outflow. Both this inner flow and the larger-scale shifts seen by S. C. Beck et al. (2020) may be related to the large-scale plume features that are prominent in the Hα image; there are multiple kinematic components seen in Hα at higher spatial resolutions that suggest this as well (A. Monreal-Ibero et al. 2010; M. S. Westmoquette et al. 2013).

5.2. Fine-structure Line Ratios and Conditions in the Sources

The three isoelemental ratios of [Ne III]/[Ne II], [S IV]/[S III], and [Ar III]/[Ar II] are calculated for each of the H II regions and are shown in Table 3. Looking at the chip as a whole, all the ratios are highest for the dominant source D1, decrease to the Ellipse, which covers the plumes, and decrease further to the whole chip. This suggests that D1 is the highest excitation and the surrounding regions add lower excitation to the total, diluting the ratios on large scales. This is borne out by the ISO and Spitzer data in larger fields: The neon and sulfur ratios for the whole chip agree with P. Beirão et al.'s (2006) results for the central 27 pc of their dithered Spitzer observations, and ISO, with apertures 14″ × 20″ and larger, found lower neon, argon, and sulfur ratios of ∼4.5, ∼2.8, and ∼1.5, respectively.

It has been established that the excitation ratios of [Ne III]/[Ne II], [S IV]/[S III], and [Ar III]/[Ar II] correlate positively with each other and negatively with metallicity (N. L. Martín-Hernández et al. 2002a; A. Verma et al. 2003; Y. Wu et al. 2006; L. K. Hunt et al. 2010). P. Beirão et al. (2006) confirmed with Spitzer data that NGC 5253 is in this low-metallicity/high-excitation class of starbursts. However, Spitzer was unable to isolate the excitation at resolutions higher than 50pc; we can here look at sources individually.

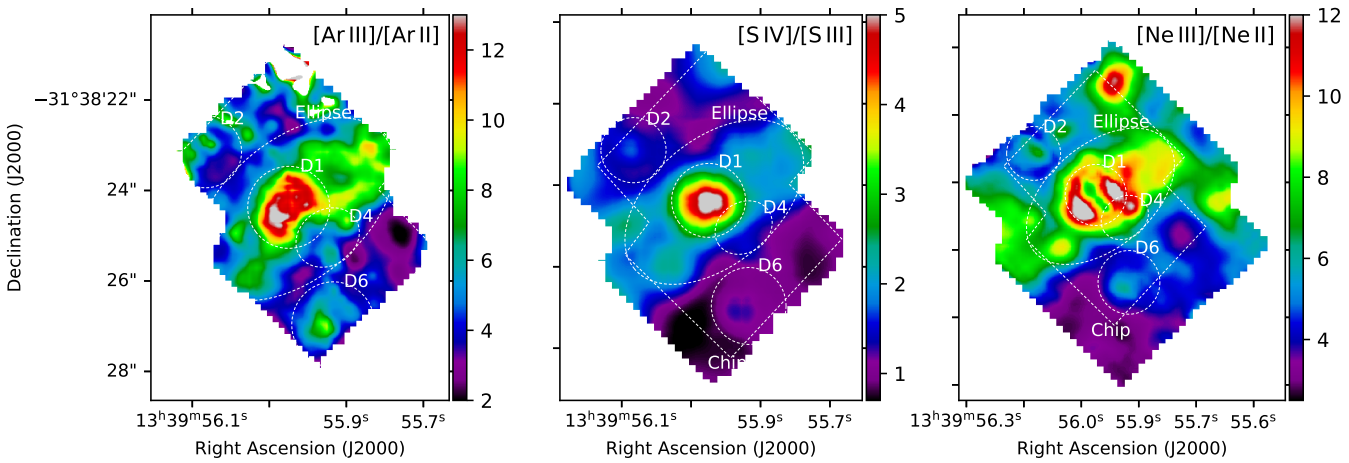


Figure 8. Isoelemental line ratios of (left to right) [Ar III]/[Ar II], [S IV]/[S III], and [Ne III]/[Ne II]. The regions from which spectra were taken are outlined in dashed lines. Continuum-free line emission maps were progressively regridded to matching scales and convolved to the PSF of the longer-wavelength line before the ratio was taken. Ratios were not computed for values less than twice the rms of the continuum-subtracted line map; this affects only the [Ar II] line, at the northern extent of the chip, apparently due to an image artifact. A sharp change in the [Ne III], the brightest line, at the supernebula also appears to be an image artifact, possibly due to saturation. By contrast, the lower [Ar III]/[Ar II] ratio at the center of D1 is due to silicate absorption of [Ar III].

Table 3
Isoelemental Lines in NGC 5253[a]

Source	[Ne III]	[Ne II]	$\frac{\text{[Ne III]}}{\text{[Ne II]}}$	[S IV]	[S III]	$\frac{\text{[S IV]}}{\text{[S III]}}$	[Ar III]	[Ar II]	$\frac{\text{[Ar III]}}{\text{[Ar II]}}$
D1	1592	167	9.53	2301	609	3.78	350	30	11.6
D2	108	20	5.4	76	54	1.4	19	3.4	5.5
D4	347	40	8.7	275	160	1.7	41	6	6.8
D6	203	46	4.4	134	129	1.0	40	6.4	6.2
Ellipse	2770	305	9.0	3420	1210	2.8	480	57	8.4
Chip	3580	434	8.25	3860	1560	2.47	584	78	7.5

Note.
[a] Units of flux are 10^{-18}W m^{-2}. Errors in the fluxes and ratios are dominated by the absolute photometric uncertainty of the system and are estimated as 4%–5% for fluxes and line ratios, with the exception of [Ar II] and the [Ar III]/[Ar II] ratio in region D2, which have 10% uncertainty.

D1 is among the highest-excitation objects known among Galactic and nearby extragalactic H II regions (U. Giveon et al. 2002; N. L. Martín-Hernández et al. 2002a; A. Verma et al. 2003; Y. Wu et al. 2006). This is in part because of the low metallicity of NGC 5253, but also because of the extraordinary luminosity of the cluster within D1. The evidence for this comes from the ratios for the lower-luminosity H II regions D2, D4, and D6, which are significantly lower in excitation but are still located in the higher-excitation half of P. Beirão et al.'s (2006) distribution.

In Figure 8 we present maps of the isoelemental line ratios. These maps were constructed by rebinning the continuum-free line images and convolving ("beam matching") the shorter-wavelength line to match the PSF of the longer wavelength. Because of image artifacts, minor features, particularly at the chip edges, must be viewed with caution in these ratio images.

Interpreted broadly, the ratio maps reflect variations in excitation and conditions across the 100 pc central region surrounding D1. The higher-excitation line in each ratio peaks near the supernebula core, D1. This is clearest for [Ne III]/[Ne II], the ions of which have the most straightforward excitation dependence, with excitation energies of 41 and 22 eV, respectively.

[Ar III]/[Ar II] is the lowest-excitation pair; the ions are created at 28 and 16 eV, respectively. From the line map of Figure 7 it is clear that the entire region is bathed in [Ar II] emission, while [Ar III] is concentrated in several clumps. The line ratio map shows that [Ar III] favors the H II regions corresponding to D1, D2, and D6, and may also suggest that other H II regions, near the edge of the chip to the north, are influencing the emission. The [Ar III]/[Ar II] ratio is high following the plumes traced by Pfα to the north and (slightly) to the south of D1 and is also elevated along other filamentary structures through much of the region. The apparent dip in the ratio at the center of D1 is consistent with silicate absorption of the [Ar III] line; the continuum indicates a silicate optical depth of $\tau_{\rm sil} \sim 0.3$ at this wavelength (J. L. Turner et al. 2026).

[S IV] and [S III] have excitation energies of 35 and 23 eV, respectively. These lines also have relatively low critical densities and begin to de-excite collisionally at densities above $n_e \sim 10^{4-4.3}$ cm^{-3}. In other words, for densities similar to those of Orion these lines will be suppressed even if the ions have been created by energetic photons. When the ratios are compared with the even higher-excitation lines of Ne, there is evidence that density is playing a role. The regions of low [S IV] (blue in Figure 7) can be seen by reference to Figure 1 to be associated with the dense and warm molecular clouds traced by the strongest CO(3–2) emission. [S IV] is strong along the plumes, as traced clearly by blue in the ratio map in Figure 8.

[Ne III]/[Ne II], the highest-excitation line pair, peaks at the supernebula core. [Ne III] has the highest line-plus-continuum

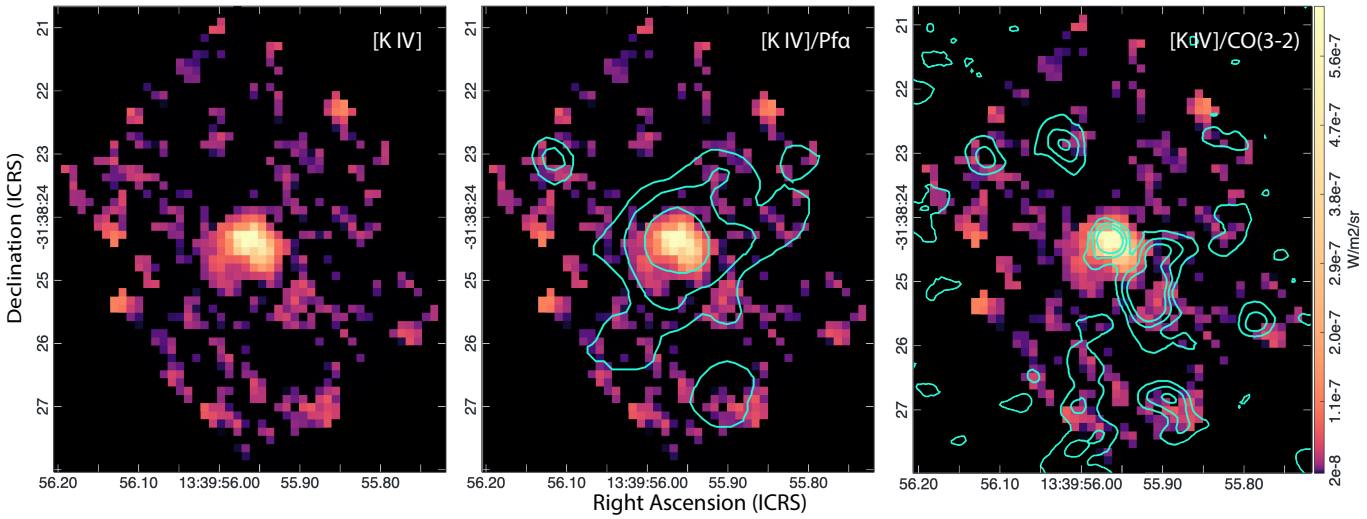


Figure 9. Integrated line intensity (MOM0) map of [K IV], shown with Pfα and CO(3–2) contours. The color bar to the right is for [K IV]. Pfα contours are (2, 4, 16) $\times 10^{-7}$ W m^{-2} sr^{-1}; CO(3–2) are (0.08, 0.32, 0.64) $\times$ Jy bm^{-1} km s^{-1}.

intensity of any of the bands, 330 GJy sr^{-1}. The line appears to show an artifact at the peak in D1, causing the ratio to be suppressed or relocated at the peak of the emission, and raised to the north, and may be due to saturation; however, this shift of the peak could also be real. (The spectral extraction regions used for the fluxes in Table 1 were chosen to be large enough to wash out this artifact among others.) The [Ne III]/[Ne II] ratio is high along the plumes, both northwest and southeast, even though the total ionization is low, indicating the escape of very high-energy photons. That this high ratio is seen in the plumes is strong evidence that, in spite of the high extinction in D1, 41 eV photons are escaping from the giant cluster within the supernebula core to distances of 50 pc and more.

Full models of the spectra from the NGC 5253 emission regions are now in progress. They will make it possible to determine the nebular and ionization parameters and deduce the stellar populations created by the starburst. A first approach with the models of J. R. Rigby & G. H. Rieke (2004) may already show the most striking features of the emission regions. Comparing the [Ne III]/[Ne II] and [Ar III]/[Ar II] ratios to J. R. Rigby & G. H. Rieke's (2004) low-metallicity models suggests that D1 is very young ($<3 \times 10^6$ yr) and that the upper mass limit for the embedded cluster is at least 50 $M_\odot$. D2 and D6 may be consistent with ages up to 5×10^6 yr and any mass limit greater than $\sim$40 $M_\odot$. D4 appears to be between the conditions of D1 and D2 but must be treated with caution because the fluxes may include emission from D1. NGC 5253 is truly an extreme starburst source.

5.3. High-excitation Lines

In the preceding section, we showed images of two high-excitation lines, [S IV] and [Ne III], with excitation potentials (EPs) of 41 and 35 eV, respectively. They are very strong in D1 and also weakly present in D2 and D6. Other very high-excitation lines detected in D1 are [Cl IV] 11.76μm, [O IV] 25.89 μm, and [K IV] 5.982μm, which have EPs of 40, 46, and 55 eV, respectively. Although [O IV] is detected in all regions except D1, [K IV], which is of similar strength and in a less noisy spectral region, is only detected in D1. We show the image of [K IV] in Figure 9. Because the continuum in D1 is so strong, we checked the continuum subtraction by making a null map by differencing the continuum images on both sides of the line, and [K IV] is significantly stronger than the null image.

[O IV] and [K IV] can be created by hot stars with hard radiation fields; they are typically seen in planetary nebulae (J. Bernard Salas et al. 2001; O. C. Jones et al. 2023). The NGC 5253-D1 cluster is not old enough for planetary nebulae to have evolved, but its youth, large stellar population, and great compactness make it likely that hot Wolf–Rayet (WR) stars or stripped stars have formed there.

We have tentatively identified the [Ne V] line in the three regions of NGC 5253 containing D1. S. Hernandez et al. (2025) recently detected [Ne V] 14.3217 μm and [Ne VI] 7.6524 μm in the starburst center of M83, which is at roughly the same distance as NGC 5253. These lines have very high EPs of 97 and 126 eV, respectively. S. Hernandez et al. (2025) argue that these lines are difficult to excite in star-forming regions, and indeed other regions of M83 have low [Ne III]/[Ne II] ratios, typical of star formation in high-metallicity, low-excitation H II regions. They thus infer the presence of an AGN in M83. In NGC 5253, we detect lines at the [Ne V] wavelength of 14.3217μm with fluxes of 2–4 $\times 10^{-18}$ W m^{-2} in the D1, Ellipse, and Chip regions. If this line were [Ne V], its velocity centroids would consistently be blueshifted by 50 km s^{-1} relative to other lines in D1, an offset not significantly greater than the uncertainty of a weak line centroid. The flux grows consistently from D1 though Ellipse to Chip, indicating that the [Ne V] flux is extended. [Ne V] 14.3217μm has been detected in an extended region in the dwarf star-forming galaxy I Zw 18 (A. Arroyo-Polonio et al. 2025; L. K. Hunt et al. 2025), but I Zw 18 has a metallicity an order of magnitude less than NGC 5253 and presumably harder radiation fields.

5.4. Contribution of Mid-infrared Lines to Total Cooling and Luminosity

The very bright MIR lines detected by MIRI/MRS contribute to the gas cooling and infrared luminosity within the starburst. In this section we compute the luminosities of the major cooling lines, determine their fractional contribution to the total infrared luminosity,

Table 4
Cooling Lines in NGC 5253

Region	$L_{\rm MIR}^{\rm est}$ ($L_\odot$)	$L_{\rm MIR}^{\rm H\,I}$ ($L_\odot$)	$L_{\rm MIR}^{\rm lines}$ ($L_\odot$)	$\frac{L_{\rm MIR}^{\rm lines}}{L_{\rm MIR}^{\rm est}}$ (%)	$\frac{L_{\rm [S\,IV]}}{L_{\rm [Ne\,III]}}$
D1	3.3×10^8	1.5×10^5	2.3×10^6	0.7	1.5
D2	3.3×10^7	7.3×10^3	1.3×10^5	0.4	0.71
D4	6.3×10^7	1.7×10^4	4.0×10^5	0.6	0.79
D6	3.3×10^7	1.4×10^4	2.6×10^5	0.8	0.66
Ellipse	6.3×10^8	2.0×10^5	3.8×10^6	0.6	1.2
Chip	7.1×10^8	2.5×10^5	4.6×10^6	0.6	1.1

Note. Uncertainties in the luminosities and ratios are dominated by the photometric uncertainty of the system and are estimated at ∼4%.

determine which are most important in the individual sources, and compare to the far-infrared (FIR) cooling lines detected in NGC 5253 by the Herschel PACS Dwarf Galaxy survey (S. C. Madden et al. 2013; D. Cormier et al. 2015). While Herschel PACs has a larger beam, $9'' \times 12''$, it can be compared to the Chip region, which is $6'' \times 7''$. For most FIR cooling lines, aside perhaps from [C II] 157 μm, the difference in aperture size is likely insignificant. In most respects, NGC 5253 has the typical FIR behavior of a dwarf galaxy (D. Cormier et al. 2015), with properties characteristic of high-excitation radiation fields and distinct from those of typical star-forming spiral galaxies.

In Table 4 we present the line luminosities, the H I line luminosities, and their relative percentage contributions to the total MIR luminosity, $L_{\rm MIR}^{\rm est}$, from Paper I. The top six cooling lines in all regions are, in order of importance, [S IV] 10.5 μm, [Ne III] 15.5 μm, [S III] 18.7 μm, [Ar III] 9.0 μm, [Ne II] 12.8 μm, and H I(6–5) 7.46 μm. In the less luminous regions D2 and D4, [Ne III] dominates and [Ne II] exceeds [Ar III] in luminosity. The top six cooling lines account for ∼90%–93% of the MIR line cooling; the top three lines, [S IV], [Ne III], and [S III], account for 75%–83% of total line cooling. H I lines account for about 5% of the line cooling; the most important contributor is Pfα (H I (6–5)). The uncertainty in all cases is dominated by the overall ∼4% calibration uncertainty.

Lines contribute ∼0.4%–1.5% to the total MIR luminosity, $L_{\rm MIR}$, in the different spatial regions. Since we have shown that the Ellipse region contains photons escaping from D1, we consider fluxes from Ellipse to be the best measure of the contribution of the massive star cluster within the D1 region. In Ellipse, lines contribute ∼0.6% to the total luminosity. D6 has the highest line contribution to its MIR luminosity, 1.5%, which may reflect the relatively low extinction of D6. Overall, lines contribute ∼0.6% of the luminosity in the entire Chip.

Line cooling is usually dominated by the strong FIR lines, but in this starburst region the MIR contribution to line cooling is significant. The total FIR line cooling for the starburst region is $7.1 \times 10^6\ L_\odot$, based on fluxes from D. Cormier et al. (2015). The FIR line cooling is dominated by the [C II] 157μm, [O I] 63μm, and [O III] 88 μm lines. This number can be compared to the MIR contribution, which is $L_{\rm MIR}^{\rm lines} = 4.4 \times 10^6\ L_\odot$. Hence, ∼38% of the total infrared line cooling of $L_{\rm IR}^{\rm lines} = 1.2 \times 10^7\ L_\odot$ is from the MIR. This is in line with the suggestion of I. De Looze et al. (2014) that the FIR lines can be less important in low-metallicity systems.

Line cooling contributes only a small fraction of the luminosity in the region. The total infrared luminosity integrated over the spectral energy distribution is $L_{\rm TIR} = 1.4 \times 10^9\ L_\odot$ (D. Cormier et al. 2015, corrected to 3.7 Mpc), of which about half is emitted in the 5–25 μm region. The total line cooling, both MIR and FIR for the central $6'' \times 7''$ region, is $1.2 \times 10^7\ L_\odot$. Line cooling represents about 1% of the total infrared luminosity in the Ellipse region; the other 99% of the luminosity is in the dust continuum.

The D1 source has the smallest MIR line luminosity fraction of 0.38%, which reflects its high internal extinction. D1 dominates the luminosity, with more than 40% of $L_{\rm TIR}$ from the starburst due to MIR emission from the D1 region. Based on the observed free–free emission, the predicted Lyα luminosity is $2 \times 10^6\ L_\odot$. If we assume that all the dust continuum emission is hot dust emitting in the MIR from within the H II region, then Lyα heating contributes about one-third of the dust luminosity in D1. For the larger Chip region, Lyα dust heating is responsible for ∼15% of the total infrared luminosity $L_{\rm TIR}$.

S. Silich et al. (2023) considered the contribution to gas heating of turbulence generated by stellar motions within the cluster as a means of explaining the unusually warm CO (J. L. Turner et al. 2015, 2017). From the properties of D1, they computed a turbulent dissipation rate of $0.4–2 \times 10^4\ L_\odot$. This turbulence will affect both ionized and neutral gas; the neutral gas cooling will be dominated by the FIR lines. Cooling by ionized gas appears to dominate in D1, with $L_{\rm ionized} \sim 6 \times 10^6\ L_\odot$, or ∼1% of the total MIR luminosity of D1, even not including any contribution from [C II] 157μm. The ionized gas cooling exceeds the turbulent heating by 2 orders of magnitude. Therefore, not surprisingly, the temperature of the gas in the H II region is determined by radiative heating.

5.5. Elemental Abundances in the NGC 5253 Starburst

Following U. Giveon et al. (2002), we address elemental abundances relative to hydrogen by comparing the infrared fine-structure lines to an infrared H I line. Our reference line is Pfα, the strongest H I line in the JWST spectra. The following equations were used:

$$\frac{\rm [Ne]}{\rm [H]} = 1.658 \times 10^{-6} \times \frac{2.30 f_{\rm Ne\,II} + f_{\rm Ne\,III}}{f_{\rm Pf\alpha}},$$

$$\frac{\rm [Ar]}{\rm [H]} = 2.203 \times 10^{-7} \times \frac{f_{\rm Ar\,II} + 1.26 f_{\rm Ar\,III}}{f_{\rm Pf\alpha}}.$$

We do not apply an ionization correction factor, since charge-exchange reactions reduce the Ar IV population, limiting higher-ionization argon, and Ne IV has such a high EP that it is unlikely to be excited. Both pairs of lines have reasonably high critical densities above $10^5\ {\rm cm}^{-3}$. We do not include sulfur because its critical densities are so low that collisional de-excitation is probable at the densities inferred from radio free–free and CO excitation in NGC 5253. Table 5 shows the abundances thus derived for all the sources. As the errors in these very strong lines are dominated by the photometric uncertainty of ∼4%, we estimate the uncertainties in the $\frac{\rm [Ne]}{\rm [H]}$ and $\frac{\rm [Ar]}{\rm [H}$ ratios to be ∼7%, and the error in 12+log[X]/[H] to be 0.01 for Ne and 0.02–0.03 for Ar.

Table 5
Abundances in NGC 5253

	D1	D2	D4	D6	Ellipse	Chip
12+log [Ne]/[H]	7.44	7.58	7.75	7.68	7.56	7.58
12+log [Ar]/[H]	5.90	5.95	5.99	6.07	5.96	5.98

Note. For each element the table shows the standard format 12 plus the log10 of the relative abundance of the element.
Uncertainties are dominated by the photometric uncertainty of ∼4%. We estimate an error of ±0.01 in 12+log([Ne]/[H]) and ±0.02–0.03 in 12+log ([Ar]/[H].

The abundances of Ne and Ar are fairly consistent across the regions. Ne is the most deviant: It is slightly underabundant by 0.7 in D1 and overabundant by 1.7 in D4. Ar is also slightly less abundant in D1 but still within the uncertainties. We have previously noted that the [Ne III] line is by far the strongest in the spectra and is associated with clear artifacts affecting both D1 and D4, so we hesitate to interpret these abundance variations.

We compare to solar values as given in K. Lodders (2021), and we find that the solar abundance of neon is 12+log([Ne]/[H]) = 8.15 and that of argon is 12+log([Ar]/[H]) = 6.5. From these values, we infer that the metallicity of NGC 5253 is 0.28 $Z_\odot$ for Ne and 0.25 $Z_\odot$ for Ar. These values are consistent with what has been determined based on other nebular lines in the region (J. R. Walsh & J.-R. Roy 1989; H. A. Kobulnicky et al. 1997; M. S. Westmoquette et al. 2013; B. G. A. Pruijt et al. 2026).

5.6. Mystery Features

An unidentified feature is seen on and close to D2. It combines emission from 14.00 to 14.02 μm with absorption between 13.969 and 13.99 μm. The width and shape of both emission and absorption features strongly suggests that they arise in a molecular band or bands. Many common interstellar molecules, most dominated by HCN, have bands around 14 μm that could contribute to a broad-line feature. The combination of emission with blueshifted absorption can be caused by an extended outflow. If this is the mechanism on D2, it implies a velocity range of 300–600 km s^{-1}, consistent with stellar outflows. Further study of D2 could determine the evolutionary state of those sources and trace the progress of star formation in this starburst.

Other absorption features are seen around 5.7μm in D1 and the regions containing it. As can be seen in Figure 2, they coincide with some strong H_2CO features. Further observations at higher spectral resolution will be necessary to identify and understand molecular features in these spectra.

6. Discussion

The goals of this project included characterizing star-forming regions in the center of NGC 5253 and determining how the massive central cluster D1 affects its surroundings. The JWST/MIRI/MRS observations agree with earlier ISO and Spitzer results that NGC 5253 is a very high-excitation source. The ratio of [Ne III]/[Ne II] exceeds 4.4–8 in all the H II regions and is ∼10 in D1, the aperture containing the massive cluster. This is one of the highest values of [Ne III]/[Ne II] seen in any starburst galaxy (N. L. Martín-Hernández et al. 2002b; A. Verma et al. 2003; Y. Wu et al. 2006), larger even than the LMC planetary nebula SMP LMC 058 (O. C. Jones et al. 2023). The ratio of [S IV]/[S III] is also highest in D1, giving a value of 3.78, compared to 1.0–1.7 for the other H II regions. The line ratios of the H II regions other than D1 resemble those of other low-metallicity star formation regions; the excitation of D1 is extreme, consistent with very massive and very young stars.

We have shown that obscuration is high around the D1 cluster, with MIR extinction A(MIR) ∼ 1.3, consistent with 30–35 mag of visual extinction. In spite of this high extinction, JWST/MIRI/MRS shows that UV photons escape from D1. In Paper I, we found that roughly 25% of the MIR and radio free–free luminosity appeared to be emitted beyond the D1 aperture. The MIRI/MRS imaging confirms that D1 is the source of the photons: The plumes seen in Hα images are also reflected in regions of high [Ne III]/[Ne II] ratio (Figure 8). Thus 50 eV photons from D1 reach distances of at least 50–60 pc from D1 in spite of the heavy extinction. This is another indication that, as suggested by CO (S. M. Consiglio et al. 2017; J. L. Turner et al. 2017), the molecular cloud in the D1 core complex has a highly clumped and porous structure that creates paths for photon escape.

The kinematic picture in this region is extremely complex. However, it is consistent with the turbulent model of the molecular core (S. Silich et al. 2023), which suggests that massive stars moving in the gravitational well of a dense star cluster will continuously stir the molecular gas, compensating for dissipation by turbulence and supporting a quasi-equilibrium state. Stellar winds and ionization fronts around the moving stars create cavities and tunnels that will expand into the lower-density regions close to the cloud edge; some cavities may break out of the cloud completely and allow the ionizing photons to escape.

Not only a porous cloud structure but active wind dynamics may be at work here, as suggested by ground-based spectroscopy, which detects a shift from red to blue across the supernebula from southeast to northwest (M. S. Westmoquette et al. 2013; D. P. Cohen et al. 2018; S. C. Beck et al. 2020), of order 13–30 km s^{-1}. The line width of the supernebula core in Brα is 65 km s^{-1}, but with a weak plateau feature extending to 150 km s^{-1}. Hα line profiles, which because of extinction must arise from a larger area, suggest that in addition to narrow-line features with shifts of 40 km s^{-1} there are also broad components (A. Monreal-Ibero et al. 2010; M. S. Westmoquette et al. 2013). These flows would have to be reconciled with the relatively placid CO gas of the D1 molecular cloud, whose 25 km s^{-1} line width is completely dominated by the stellar orbits within D1 (J. L. Turner et al. 2017). It is clear that the kinematic picture in this region is extremely complex.

Photon escape may also explain how optical and UV tracers of WR stars are seen even from this highly obscured region. (P. S. Conti 1991; D. Schaerer et al. 1997). GMOS-IFU observations of M. S. Westmoquette et al. (2013) detect a "red WR bump" spectral feature at 0.5765–0.5875 μm. Their image shows that the red WR bump appears to spatially coincide with D2 and D6 and with a plume north of D1. B. G. A. Pruijt et al. (2026) isolate the well-known nitrogen enhancement to this region immediately to the north of D1. This suggests mass dispersal by winds through holes in the D1 cloud/cluster. Although D6 has lower MIR extinction than the other H II regions, D2 has high MIR extinction, and the detection of WR

features there may also indicate porosity. The WR feature in the northern plume almost certainly originates in D1 and has escaped through the clumpy and porous gas there. Thus the spectroscopic signatures of WR stars can provide important clues to the stellar content of these embedded clusters in spite of the very high visual obscuration.

7. Conclusions

We have presented here an overview of the rich emission-line spectrum measured by JWST for the starburst in NGC 5253 to follow on a study of the continuum sources presented in Paper II (J. L. Turner et al. 2026). We present fluxes and velocities for more than 70 lines, measured in six different apertures, including the supernebula core, NGC 5253-D1, and three other H II regions and MIR continuum sources, NGC 5253-D2, NGC 5253-D4, and NGC 5253-D6. We have derived the extinction law and total obscuration based on 30 H I lines detected from four different series. From the fluxes of the strong fine-structure lines of [Ar II] 6.99 μm, [Ar III] 8.99 μm, [Ne II] 12.8 μm, [Ne III] 15.5 μm, [SIII] 18.7 μm, and [S IV] 10.5 μm, we made "first pass" estimates of conditions in the four embedded H II regions, including the supernebula D1 and the less luminous D2, D4, and D6 regions that were defined in Paper I. We find as follows.

1. The extinction derived from ratios of H I recombination lines and the free–free radio continuum is almost flat from 5 to 20 μm, as it is in the Galaxy.
2. The extinctions for the different regions can be significant, even in the MIR. Mid-infrared extinctions derived for the H II regions are A(MIR) $= 1.3 \pm 0.2$ for D1 (supernebula core), 0.58 ± 0.2 for D2, and consistent with zero for D4 and D6. These correspond to visual extinctions of $A_v = 35$ mag for D1 and 18 mag for D2. Visual extinction could be as high as 5 mag for D4 and D6, although the MIR results are also consistent with $A_v = 0$ for those sources. Considering fluxes over the whole central region, the observed extinction is lower than in D1, at 0.9–1.0 mag.
3. The Galactic relation between A_v and the depth of the silicate feature $\tau_{9.7}$ does not hold; the silicate feature in D1 is weaker than predicted by factors of $\sim$5.
4. The isoelemental line ratios, particularly [Ne III]/[Ne II], as well as the detection of [K IV] 5.98μm, [Ne V] 14.32μm, and [O IV] 25.89 μm, show that the embedded cluster source D1 has extremely high excitation, consistent with very massive ($\sim$100 $M_\odot$) stars at very young ages. This demonstrates that the high ratios in D1 are in part due to a large young stellar population ($L \sim 10^9\, L_\odot$) within the $r \sim$ 1–2 pc supernebula core, but in part also due to the low metallicity of the galaxy, since the smaller ($L \sim 10^7\, L_\odot$) H II regions also have high excitation.
5. We compute a total cooling rate from the MIR lines of $4.6 \times 10^6\, L_\odot$ for the entire MRS $6'' \times 7''$ footprint, about half the cooling rate from the FIR lines (D. Cormier et al. 2015), so MIR lines are significant contributors to cooling. The MIR lines contribute $\sim$0.4%–0.8% of the MIR luminosity in the different regions.
6. We compute abundances for neon, 12+log([Ne]/[H]) = 7.4–7.74, and argon, 12+log([Ne]/[H]) = 5.9–6.0. We do not see notable spatial trends; the D1 abundances tend to be slightly low, but within the uncertainties. These values are consistent with previous work showing that the nebular metallicity of NGC 5253 is $\sim$0.3 $Z_\odot$.
7. Images of the isoelemental line ratios show that photons with energies as high as 46 eV are escaping the D1 supernebula core and reaching distances of at least 50 pc from the cluster, in spite of the very high ($A_v \sim$ 30–35) visual extinction. Based on the distribution of free–free emission, we estimate that $\gtrsim$25% of the photons escape D1 (J. L. Turner et al. 2026). This, with evidence of clumpiness in the CO (S. M. Consiglio et al. 2017; J. L. Turner et al. 2017), suggests that the interior of this deeply embedded cloud/cluster is clumpy and porous and allows shorter-wavelength spectroscopic signatures, such as WR features, to be seen.

Acknowledgments

We thank the JWST Help Desk for their substantial assistance with the data, including Boris Trahin and David Law among others.

Data Availability

JWST data used in this paper can be found in MAST (doi:10.17909/xa2a-8m80).

Facilities: JWST (MIRI-MRS), IRSA, NED, ALMA.

Software: astropy (Astropy Collaboration et al. 2013, 2018, 2022), R (R Core Team 2023), Cloudy (G. J. Ferland et al. 2017), jdaviz (J. Developers et al. 2025), CARTA (A. Comrie et al. 2025), AIPS (E. W. Greisen 1990).

Appendix

The full spectra of each of the five regions discussed are shown below (Figures 10–14) in detail. Each spectrum is displayed in 12 panels, one panel for each wavelength band of the spectrometer, and with intensity scales adjusted to the source brightness in each band. The wavelengths of lines detected and listed in Table 1 are marked in red.

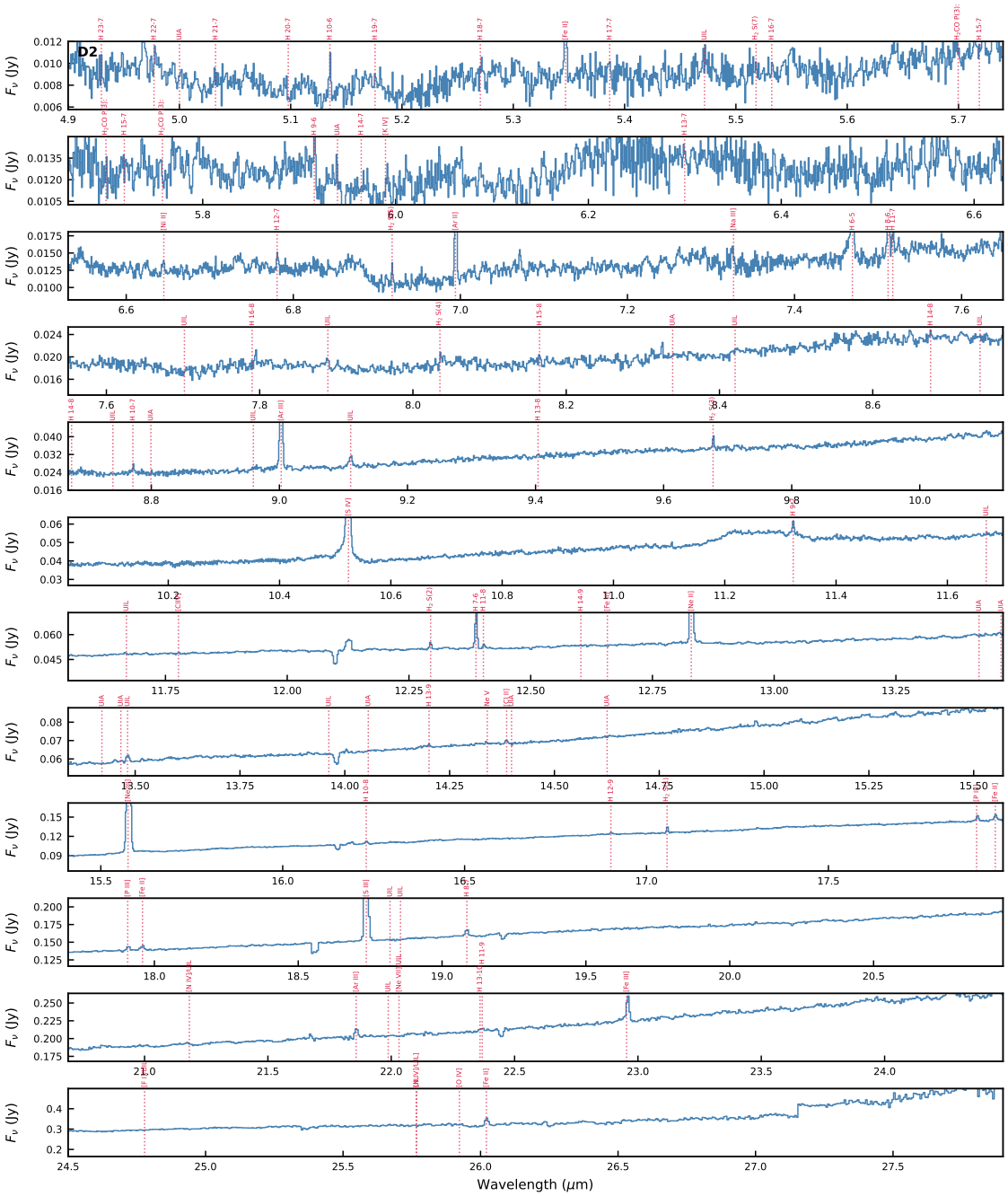


Figure 10. Full spectrum of region D2 in a 0.″8 beam. D2 is very near the edge of the MRS footprint, and it extends beyond it for the shorter wavelengths. The abrupt features and lacunae are likely due to edge effects and are not seen in the other regions.

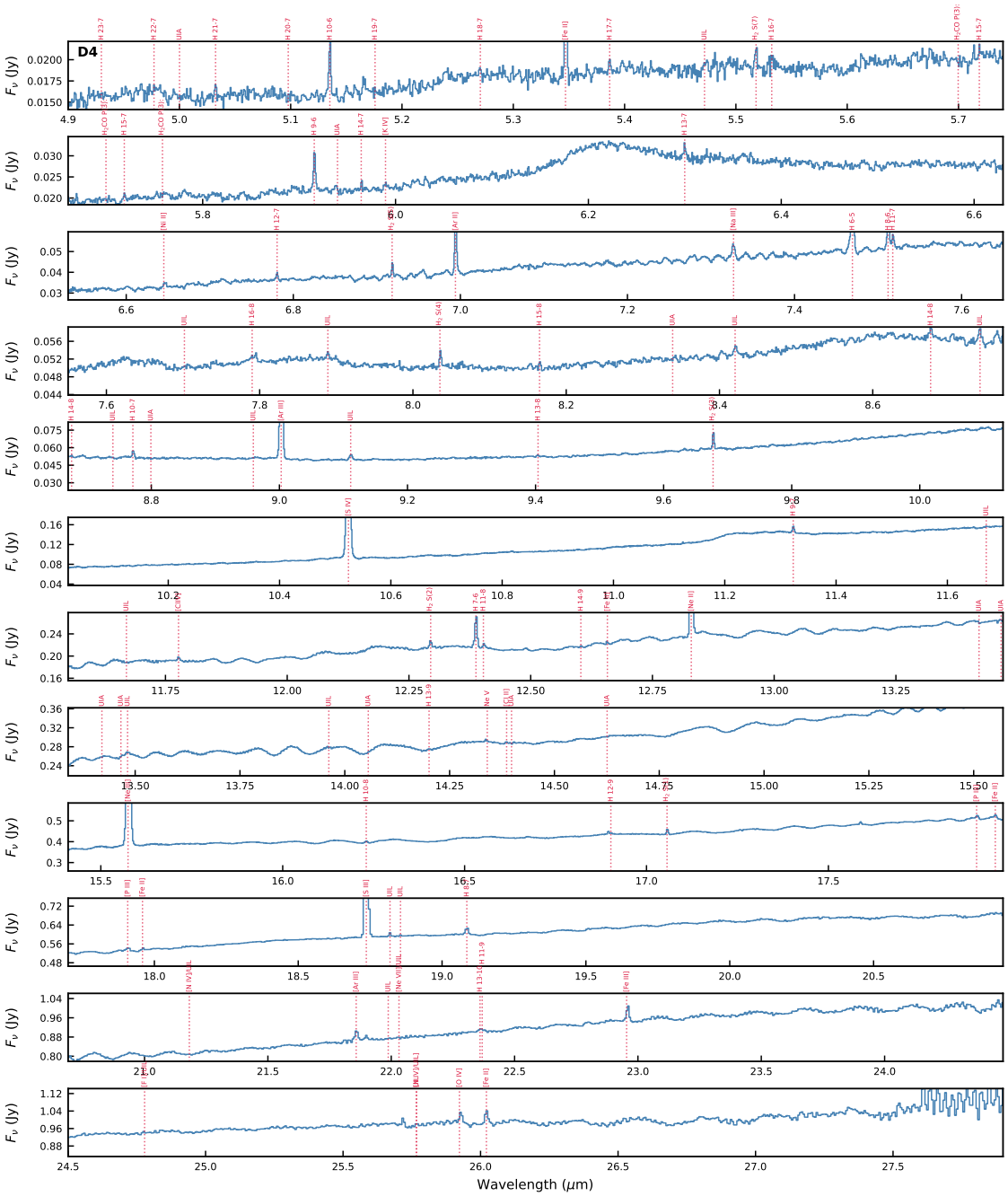


Figure 11. Full spectrum of region D4 in a $0\farcs6 \times 0\farcs7$ beam. D4 is very close to the supernebula and is affected by the PSF and fringing.

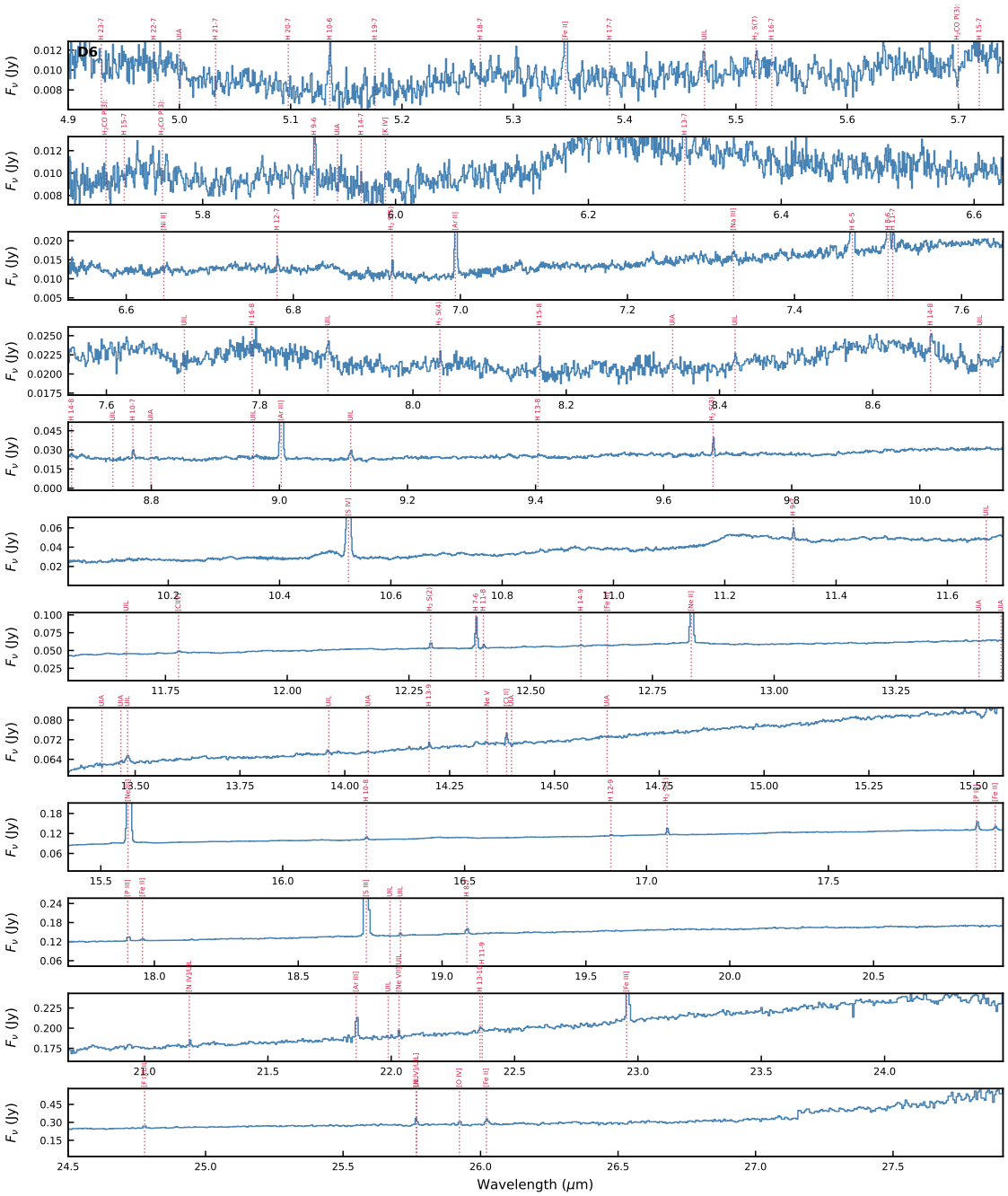


Figure 12. Full spectrum of region D6 in a 0.″9 beam.

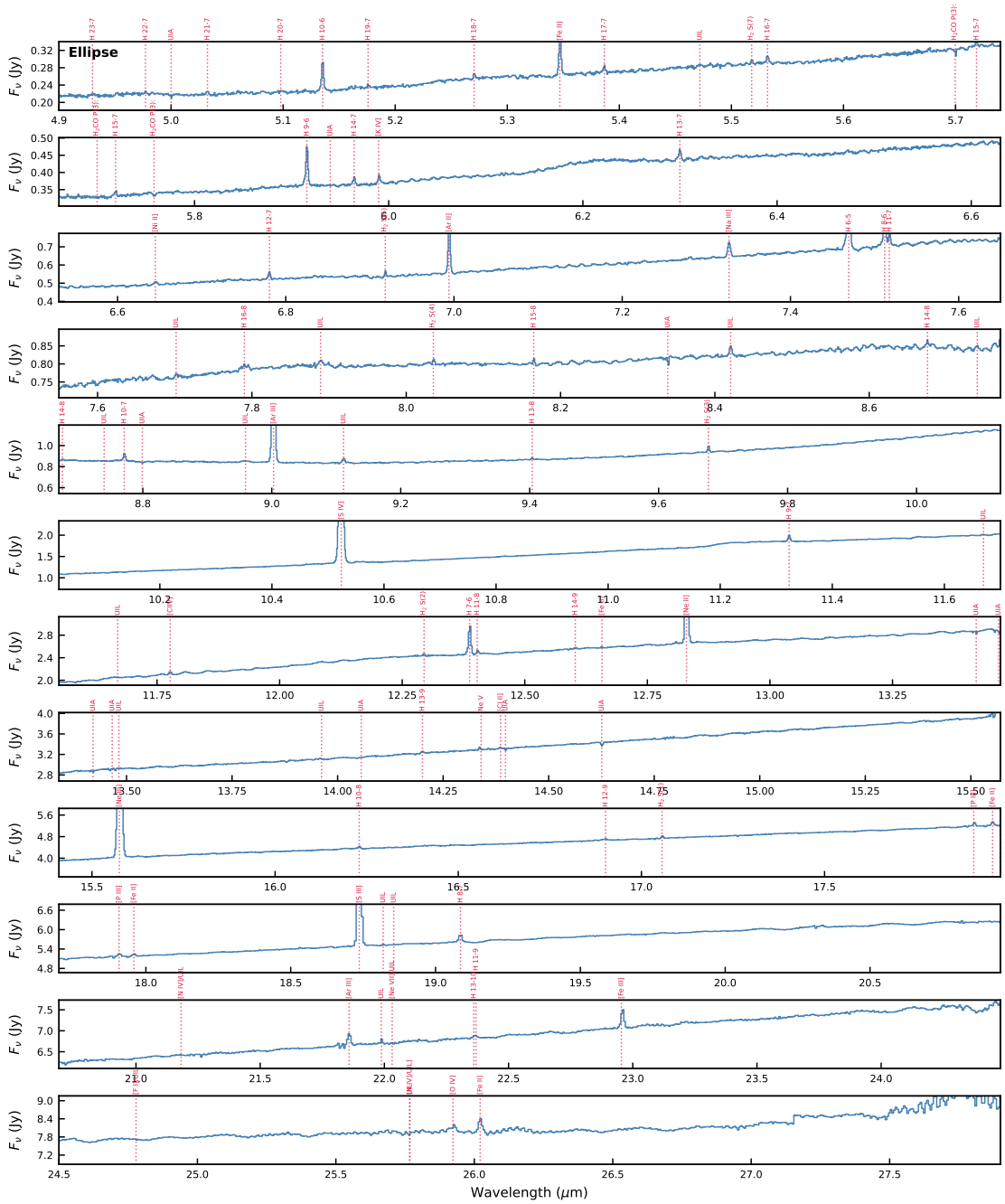


Figure 13. Full spectrum of the Ellipse region.

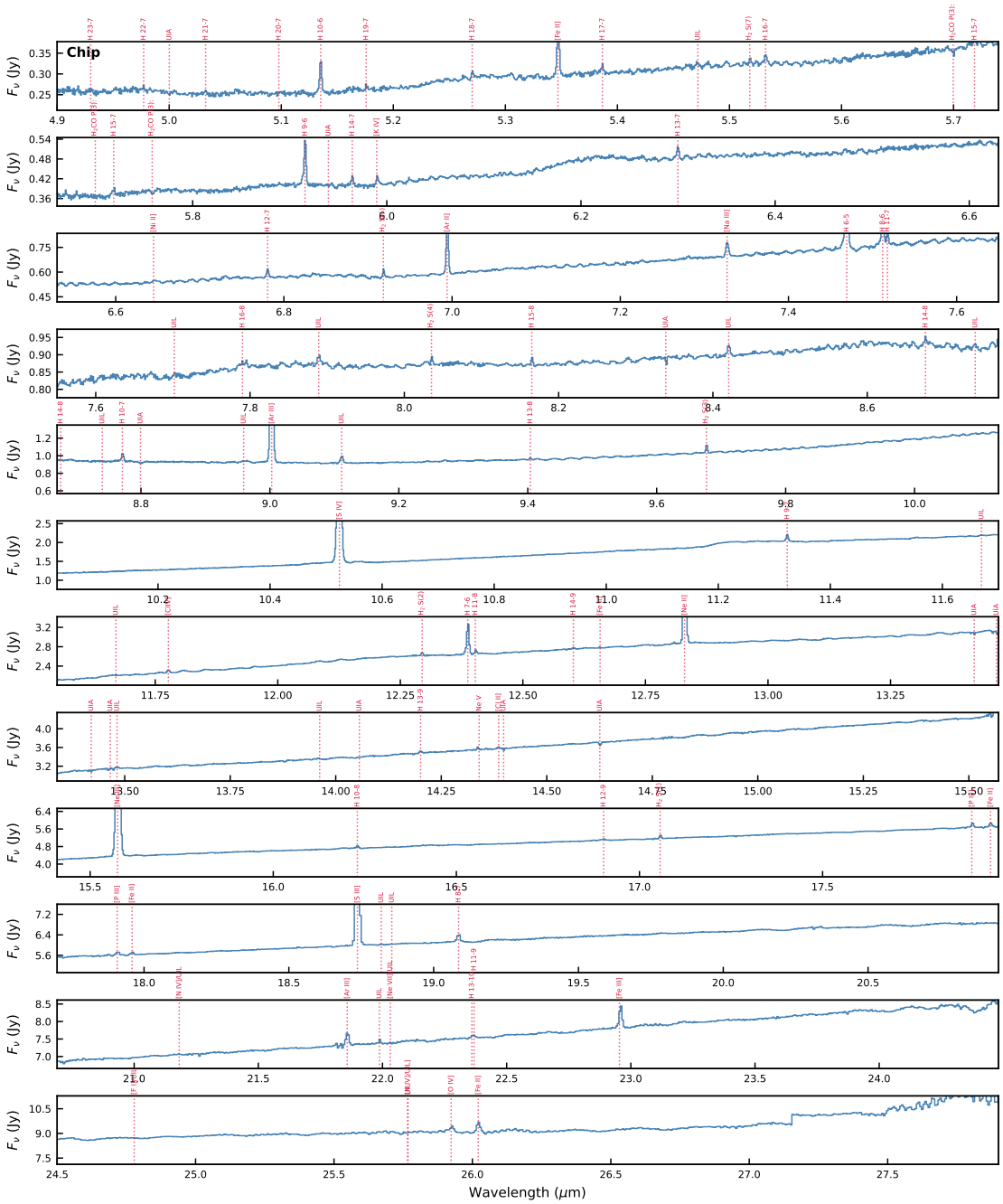


Figure 14. Full spectrum of the entire Chip; the area covered will depend on the wavelength, as shown in the text.

ORCID iDs

Sara C. Beck https://orcid.org/0000-0002-5770-8494
Jean L. Turner https://orcid.org/0000-0003-4625-2951
Elm Zweig https://orcid.org/0000-0001-5678-7509
John H. Black https://orcid.org/0000-0001-7221-7207
Paul T. P. Ho https://orcid.org/0000-0002-3412-4306
David S. Meier https://orcid.org/0000-0001-9436-9471
Sergiy Silich https://orcid.org/0000-0002-3814-5294
Daniel P. Cohen https://orcid.org/0000-0002-5221-2342
S. Michelle Consiglio https://orcid.org/0000-0002-0214-0491
Nicholas G. Ferraro https://orcid.org/0000-0002-9064-4592

References

Alonso-Herrero, A., Takagi, T., Baker, A. J., et al. 2004, ApJ, 612, 222
Argyriou, I., Glasse, A., Law, D. R., et al. 2023a, A&A, 675, A111
Argyriou, I., Lage, C., Rieke, G. H., et al. 2023b, A&A, 680, A96
Arroyo-Polonio, A., Kehrig, C., Vílchez, J. M., et al. 2025, ApJL, 987, L36
Astropy Collaboration, Price-Whelan, A. M., Lim, P. L., et al. 2022, ApJ, 935, 167
Astropy Collaboration, Price-Whelan, A. M., Sipőcz, B. M., et al. 2018, AJ, 156, 123
Astropy Collaboration, Robitaille, T. P., Tollerud, E. J., et al. 2013, A&A, 558, A33
Beck, S. C., Lacy, J., Turner, J., et al. 2020, MNRAS, 497, 1675
Beck, S. C., Turner, J. L., Ho, P. T. P., Lacy, J. H., & Kelly, D. M. 1996, ApJ, 457, 610
Beirão, P., Brandl, B. R., Devost, D., et al. 2006, ApJL, 643, L1
Bendo, G. J., Miura, R. E., Espada, D., et al. 2017, MNRAS, 472, 1239

Bernard Salas, J., Pottasch, S. R., Beintema, D. A., & Wesselius, P. R. 2001, A&A, 367, 949
Calzetti, D., Johnson, K. E., Adamo, A., et al. 2015, ApJ, 811, 75
Calzetti, D., Meurer, G. R., Bohlin, R. C., et al. 1997, AJ, 114, 1834
Cesarsky, D., Jones, A. P., Lequeux, J., & Verstraete, L. 2000, A&A, 358, 708
Chiar, J. E., & Tielens, A. G. G. M. 2006, ApJ, 637, 774
Cohen, D. P., Turner, J. L., Consiglio, S. M., Martin, E. C., & Beck, S. C. 2018, ApJ, 860, 47
Comrie, A., Wang, K.-S., Hwang, Y.-H., et al. 2025, CARTA: The Cube Analysis and Rendering Tool for Astronomy, v5.0, Zenodo, doi:10.5281/zenodo.17050846
Consiglio, S. M., Turner, J. L., Beck, S., et al. 2017, ApJ, 850, 54
Conti, P. S. 1991, ApJ, 377, 115
Cormier, D., Madden, S. C., Lebouteiller, V., et al. 2015, A&A, 578, A53
Decleir, M., Gordon, K. D., Andrews, J. E., et al. 2022, ApJ, 930, 15
De Looze, I., Cormier, D., Lebouteiller, V., et al. 2014, A&A, 568, A62
Developers, J., Averbukh, J., Bradley, L., et al. 2025, Jdaviz, v4.4.1, Zenodo, doi:10.5281/zenodo.17211099
Dicken, D., Marín, M. G., Shivaei, I., et al. 2024, A&A, 689, A5
Draine, B. T. 2011a, Physics of the Interstellar and Intergalactic Medium (Princeton Univ. Press)
Draine, B. T. 2011b, ApJ, 732, 100
Ferland, G. J., Chatzikos, M., Guzmán, F., et al. 2017, RMxAA, 53, 385
Gáspár, A., Rieke, G. H., Guillard, P., et al. 2021, PASP, 133, 014504
Giveon, U., Sternberg, A., Lutz, D., Feuchtgruber, H., & Pauldrach, A. W. A. 2002, ApJ, 566, 880
Gordon, K. D., Clayton, G. C., Decleir, M., et al. 2023, ApJ, 950, 86
Gordon, K. D., Misselt, K. A., Bouwman, J., et al. 2021, ApJ, 916, 33
Greisen, E. W. 1990, in Acquisition, Processing and Archiving of Astronomical Images, ed. G. Longo & G. Sedmak (Osservatorio Astronomico), 125
Guseva, N. G., Izotov, Y. I., Stasińska, G., et al. 2011, A&A, 529, A149
Harris, J., Calzetti, D., Gallagher, J. S. I., Smith, D. A., & Conselice, C. J. 2004, ApJ, 603, 503
Hernandez, S., Smith, L. J., Jones, L. H., et al. 2025, ApJ, 983, 154
Hunt, L. K., Aloisi, A., Navarro, M. G., et al. 2025, ApJ, 992, 48
Hunt, L. K., Thuan, T. X., Izotov, Y. I., & Sauvage, M. 2010, ApJ, 712, 164
Indebetouw, R., Mathis, J. S., Babler, B. L., et al. 2005, ApJ, 619, 931
Jones, O. C., Álvarez-Márquez, J., Sloan, G. C., et al. 2023, MNRAS, 523, 2519
Kobulnicky, H. A., Skillman, E. D., Roy, J.-R., Walsh, J. R., & Rosa, M. R. 1997, ApJ, 477, 679
Lai, T. S. Y., Duval, S., Smith, J. D. T., et al. 2025, ApJL, 991, L56
Lai, T. S. Y., Smith, J. D. T., Peeters, E., et al. 2024, ApJ, 967, 83
Law, D. R., E. Morrison, J., Argyriou, I., et al. 2023, AJ, 166, 45
Lebofsky, M. J., & Rieke, G. H. 1979, ApJ, 229, 111
Lodders, K. 2021, SSRv, 217, 44
López-Sánchez, Á. R., Esteban, C., García-Rojas, J., Peimbert, M., & Rodríguez, M. 2007, ApJ, 656, 168
Lutz, D., Feuchtgruber, H., Genzel, R., et al. 1996, A&A, 315, L269
Lutz, D., Kunze, D., Spoon, H. W. W., & Thornley, M. D. 1998, A&A, 333, L75
Madden, S. C., Rémy-Ruyer, A., Galametz, M., et al. 2013, PASP, 125, 600
Martín-Hernández, N. L., Schaerer, D., & Sauvage, M. 2005, A&A, 429, 449
Martín-Hernández, N. L., Vermeij, R., Tielens, A. G. G. M., van der Hulst, J. M., & Peeters, E. 2002a, A&A, 389, 286
Martín-Hernández, N. L., Peeters, E., Morisset, C., et al. 2002b, A&A, 381, 606
Meier, D. S., Turner, J. L., & Beck, S. C. 2002, AJ, 124, 877
Monreal-Ibero, A., Vílchez, J. M., Walsh, J. R., & Muñoz-Tuñón, C. 2010, A&A, 517, A27
Monreal-Ibero, A., Walsh, J. R., & Vílchez, J. M. 2012, A&A, 544, A60
Natta, A., & Panagia, N. 1984, ApJ, 287, 228
Pruijt, B. G. A., Monreal-Ibero, A., Weilbacher, P. M., et al. 2026, MNRAS, 549, stag794
R Core Team 2023, R Foundation for Statistical Computing, Vienna, Austria, https://www.R-project.org/
Rigby, J. R., & Rieke, G. H. 2004, ApJ, 606, 237
Rodríguez-Rico, C. A., Goss, W. M., Turner, J. L., & Gómez, Y. 2007, ApJ, 670, 295
Schaerer, D., Contini, T., Kunth, D., & Meynet, G. 1997, ApJL, 481, L75
Silich, S., Turner, J., Mackey, J., & Martínez-González, S. 2023, ApJL, 944, L32
Smith, J. D. T., Draine, B. T., Dale, D. A., et al. 2007, ApJ, 656, 770
Smith, L. J., Bajaj, V., Ryon, J., & Sabbi, E. 2020, ApJ, 896, 84
Spoon, H. W. W., Marshall, J. A., Houck, J. R., et al. 2007, ApJL, 654, L49
Storey, P. J., & Hummer, D. G. 1995, MNRAS, 272, 41
Turner, J. L., & Beck, S. C. 2004, ApJL, 602, L85
Turner, J. L., Beck, S. C., Benford, D. J., et al. 2015, Natur, 519, 331
Turner, J. L., Beck, S. C., Crosthwaite, L. P., et al. 2003, Natur, 423, 621
Turner, J. L., Beck, S. C., Zweig, E. A., et al. 2026, ApJ, 1011, 203
Turner, J. L., Consiglio, S. M., Beck, S. C., et al. 2017, ApJ, 846, 73
Verma, A., Lutz, D., Sturm, E., et al. 2003, A&A, 403, 829
Walsh, J. R., & Roy, J.-R. 1989, MNRAS, 239, 297
Westmoquette, M. S., James, B., Monreal-Ibero, A., & Walsh, J. R. 2013, A&A, 550, A88
Whelan, D. G., Lebouteiller, V., Galliano, F., et al. 2013, ApJ, 771, 16
Whittet, D. C. B. 1992, Dust in the Galactic Environment (IOP Publishing)
Wu, Y., Charmandaris, V., Hao, L., et al. 2006, ApJ, 639, 157